Title
Early Brain Tumor Detection by Early Glioblastoma Modeling and Quantum Fixed-Point MR Imaging

Author
Tsai, Shang-Lin

Publication Date
2018

UNIVERSITY OF CALIFORNIA

Los Angeles

Early Brain Tumor Detection by Early Glioblastoma Modeling and Quantum Fixed-Point MR Imaging

A dissertation submitted in partial satisfaction of the

requirements for the degree Master of Science

in Chemistry

by

Shang-Lin Tsai

2018

ABSTRACT OF THE DISSERTATION

Early Brain Tumor Detection by Early Glioblastoma Modeling and

Quantum Fixed-Point MR Imaging

by

Shang-Lin Tsai

Master of Science in Chemistry

University of California, Los Angeles, 2018

Professor Yung-Ya Lin, Chair

Magnetic Resonance Imaging has been introduced for several decades; however, it is still difficult to distinguish the turmeric cell from the surrounding healthy cell at early stage due to the similarity of the micro environments. People are usually too late when they recognize their disease. My research goal is to model the difference in tumor cells' environment and explore a new way to discover the disease. To achieve that, one of the fMRI technique (Blood Oxygenation Level Dependent--BOLD) together with Monte Carlo simulation of tumor cell and healthy cell were generated, and the results were comparable with *in-vivo* mouse model. In the second part, a new approach of quantum fixed-point spin dynamic was found to be profound on enhancement of contrast between

healthy and tumor cell in MRI. With the designed pulse sequence, the home-build active feedback-controlled electronic device can differentiate the almost indistinguishable resonance offset from tumor cell and accelerate the magnetization towards the unique stable fixed points. Lastly, the spin dynamic under the active feedback source and the spin evolution under natural damping was analyzed in order to improve the understanding of the fixed points and allow for better modification of pulse sequence.

The dissertation of Shang-Lin Tsai is approved.

Michael Albert Thomas

William M Gelbart

Yung-Ya Lin, Committee Chair

University of California, Los Angeles

2018

TABLE OF CONTENTS

LIST OF SYMBOLS

O: upper-case oh

o: lower-case oh

0: zero

l: ell

1: one

M_0: upper-case em (italicized) sub zero

B_0: upper-case bee (italicized) sub zero

B_1: upper-case bee sub one

γ: gamma (Greek)

ψ: psi (Greek)

δ: delta (Greek)

ω: omega (Greek)

ν: nu (Greek)

Γ: upper-case gamma (Greek)

σ: sigma (Greek)

$\equiv$: equivalent to (Symbol)

ω_0: omega sub zero (Greek)

ω_1: omega sub one (Greek)

$\langle$: left angular bracket (Symbol)

$\rangle$: right angular bracket (Symbol)

<: less than

τ: tau (Greek)

τ_r: tau sub ar (Greek)

τ_1: tau sub one (Greek)

η: eta (Greek)

θ: theta (Greek)

ϕ: phi (Greek)

$^\circ$: degree (Symbol)

ε: epsilon (Greek)

$\times$: times (Symbol)

x: ecks

$\sim$: tilde

μ: mu (Greek)

T_2: upper-case tee sub two

$T_{1\rho}$: upper-case tee sub one sub rho (Greek)

ACKNOWLEDGEMENTS

I would like to express my great appreciation toward all my family to never stop encouraging and supporting me to pursue my academic goal in each step of my school life. Their warmest and kindest accompany made my way to reach my success much faster than what I could expect.

I also would like to thank for all the greatest and strongest support from my beloved Professor, Yung-Ya Lin, who always provided me with the best resources and directed me to develop the field what I never thought I could really reach. In my past 4 years of studying at UCLA, his spirit toward the field of science motivated me a lot on keep following his guidance of doing the research, and his inspiration even made me experience much more than I could image in the field. He is such an important figure in my life who is not only my professor, but also my role model who I always would like to become to. Because of his accompany and great support, I could start my journey on Chemistry studies, experience researches with right direction, met the great people from my lab team, and make my goal one step by another until today's stage. His spirit and motivation were my strongest supports to encourage me to walk until today's success.

Two of the other important figures, Professor Gelbart and Justyna, I also would like to express my great appreciation toward their assistances in helping me with the academic guidance and advising me in classes selection. Because of their greatest support on my

academic matters, I could fully focus on my learning without any interruption to proceed to each single stage successfully.

Professor Li, was also another significant one I would like to thank, who always gave me so much supports on both of my undergraduate and graduate studies. She was not only my best TA in my undergraduate classes learnings, but also my great mentor who always guide me to learn and find the result of the questions in the most accurate way. Without her great supports, I could not reach the academic success as I am now.

I also would like to thank specially to Guan Wang to co-authored chapter 2 and 4 with me (both chapters are in preparation for publication) as we worked separately and checked the identity of our results. Also, I would like to thank to Professor Furuyama who is the first author of chapter 3 to allow me identified, reproduced, and revised his work.

Finally, I would like to thank for the great sponsored support of the funding as bellowed: Raymond & Dorothy Wilson Research Fellowship (Summer 2017), Governor Merriam Scholarship (2015), and Norman Smith Scholarship (2015). Also, the research work was supported by the Camille and Henry Dreyfus Foundation (TC-05-053), National Science Foundation (DMS-0833863, CHE-1112574, and CHE-1416598), Hirshberg Foundation for Pancreatic Cancer Research, and Taiwan Ministry of Science and Technology (NSC 100-2113-M-002-008 and NSC 101-2113-M-002-018).

CHAPTER 1

1.1 INTRODUCTION

In the past few decades, Magnetic Resonance Imaging (MRI) has become one of the most practical ways for medical diagnosis. The use of strong magnetic fields and low-energy radiofrequency pulse in MRI scans through the organs inside the body and allows the important message such as the spin relaxation time constants (functional MRI) or absorption/emission spectrum (MR spectrum) to deliver back. The advantage of not involving toxic ionizing radiation provide a healthy way to diagnose people's body condition. MRI uses the response of nuclear spins to the different magnetic field environments, such as tumor cell, to characterize various tissue types, providing detailed anatomic information. Furthermore, functional MRI (fMRI) uses the intrinsic signal-change of NMR to develop and enhance the contrast in magnetic susceptibility such as cerebral blood volume mapping (CBV), position emission tomography (PET), and blood oxygenation level-dependent imaging (BOLD). While MRI provides extensive information on local tissue environment, it is hard to differentiate signals from similar micro conditions such as early tumor and its surrounding healthy cell. Therefore, without any indication of cancerous activity and specification on diagonalization, tumors usually remain undetected until an unstoppable growth of itself. As a result, the goal of my research is to set up an early-stage tumor cell model by simulating its micro condition and surrounding and evolving the model under the earlier found "Active Feedback Magnetic Resonance" to enhance the contrast of the cancer cell in MRI.

We presented our first model of early tumor by simulating its micro condition via blood oxygenation level dependent (BOLD). The paramagnetic property of deoxyhemoglobin particles inside the blood vessel produce a local field to its surrounding molecules. These induced field will constructively or destructively interact with the particles and shift their resonance offset. By Valable et al, it was overserved that the vessel density decreases together with the increase of vessel size during the early stage of tumor growth. Therefore, we presented the healthy cell model as nine cylinders of blood vessel and tumor cell model as one cylinder with corresponding vessel sizes, and the other parameters remained controlled. Next, we performed a Monte Carlo simulation by allowing thousands of spin particles to be randomly positioned and evolved under the given field based on the distance to the vessel. As the spins relax through transverse plane, the overall magnetization can be recorded, and the contrast of magnetizations from both health and tumor models are studied. In here, we introduced three kinds of pulse sequences from spin echo, spin locking, and CPMG to enhance the contrast between the two. We also collected the data by using three different methods: phase accumulation method, and methods of analytical and numerical solutions to Bloch equation. All the data showed strongly agreement to each other and also the in vivo experiment which was done by imaging over thirty mice which were orthotopically inoculated with GBM cells.

While it is important to have a correct model for tumor detection, the strategy of MRI enhancement is the goal for my research. The method of quantum fixed-point spin dynamics has been introduced in our group, and the experimental result showed a profound contrast in MR imaging. By Lenz's law, an oscillating current in a coil will induce indirectly by a change of magnetic flux, and the reactionary field will act back

onto the sample. Using this idea, our homebuilt active feedback field electronic device can filter, phase shift and amplify the receiving signal to respond and control the RF transmission coil in novel ways. In here, we analyzed the active feedback field in a quantum approach. In a two spin components system, the additional active feedback field, which is applied 90° indirectly and perpendicular to the transverse magnetization, increase the total energy of original state. With the constant perturbation of the weak continuous wave (CW), spins even with small difference in resonance offset will naturally evolve to different stable fixed points or constants of motion, thermodynamically. Hence, the resulting difference of the magnetization can light up the region of interest.

Lastly, the dynamics en route to the fixed points can be useful for imaging contrast and later pulse sequence design purpose. The natural/electronic radiation damping of the feedback field is governed by four parameters: the strength of CW and active feedback field, the resonance offset, and the applied phases. The contribution of the four factors produce an uneven Rabi cycle, and the spins will eventually evolve to the fixed points or constants of motion. In addition, we have analyzed and extended the understanding of fixed point dynamic to uneven contribution cases and enlarge the size to multiple components as considering more realistic situations.

As for my short-term goal, the earlier tumor model will be evolved under the presented quantum fixed-point spin dynamic, and the idea will be further used for the construction of a better design of pulse sequence. As for the long, a stronger contrast enhancement will be enriched which leads to the development of MR medicine.

CHAPTER 2

Detection of Early Glioblastoma Multiform in Orthotopic Xenograft Mouse Models: Numerical Simulations and *In Vivo* Experiments

2.1 ABSTRACT

Purpose. Investigation of blood vessel aggregation effects on MRI methods via simulation on early brain tumor (glioblastoma multiform) models proposed based on previous experimental data on vessel densities.

Methods. Monte Carlo simulation of evolution of magnetization of diffusing protons by analytical solutions of the Bloch equation, phase accumulation, and numerical methods provided by Matlab (The Mathworks Inc.).

Results. Degree of aggregation of blood vessels in the BOLD model is proportional to the relaxation speed of proton ensembles. Pulse sequences that refocus magnetization more frequently delay the relaxation speed. Simulation and *in vivo* results show reasonable agreements.

Conclusion. A new BOLD model of early brain tumor is proposed and is validated via simulation results that display trends that agree with *in vivo* results qualitatively.

2.2 INTRODUCTION

Tumor detection of early stage cancer cell still remains unclear, and it is usually too late when people found the disease of themselves. Several analytical methods of functional magnetic resonance (fMRI), such as cerebral blood volume mapping (CBV), position emission tomography (PET), and blood oxygenation level-dependent imaging (BOLD), have been studied for decades, in which fMRI uses intrinsic signal-change of NMR to develop and enhance the contrast in magnetic susceptibility. Thus we propose the first models for early tumor and healthy brain tissue inspired by (1) in which the relationship between transverse relaxation, pulse sequences used for imaging, and vessel distributions can be evaluated. In this paper, Monte Carlo simulations on the proposed models together with *in vivo* BOLD imaging have been generated for both healthy and tumor cell via the fact that in blood vessel, paramagnetic deoxyhemoglobin produces local magnetic field. These induced inhomogeneous magnetic fields around protons shift resonance frequencies and facilitate contrasts. After being evaluated via both simulations and experiments, the models can be further revised and used to conduct quantitative studies in scenarios relevant to early stage brain tumor.

There are three parts of this research. In the first part, a BOLD model for the magnetic environments of both healthy and cancer cells is proposed as infinite cylinders in a voxel cube by assuming that these identical voxels are periodic in the piece of brain we examined. From experimental results, we define our early tumor model with the time frame about 15 days from the tumor cell being implanted, and it is assumed that the edema has not yet formed. The model parameters were chosen from in vivo experiment

[2-6]. In particular, by Valable *et al.* [2], it was observed that the vessel density decreases together with the increase of vessel size during the early stage of tumor growth. Therefore, we present the healthy cell model as nine cylinders and tumor cell model as one cylinder with corresponding vessel sizes, and the other parameters remained controlled. In addition, the effect of water molecules entering and exiting blood vessel membranes is too small to be significant, and the membranes are taken to be impenetrable.

In the second part, we present Monte Carlo simulation results of magnetization relaxation in the proposed model obtained via three different methods under three pulse sequences - spin echo (SE), CPMG, and spin locking (SL). As shown in Figure 1, the relaxation of transverse magnetization of a proton depends on the dipolar field gradient changes as it diffuses randomly over time. Then under this model we are able to evaluate the vessel density and pulse sequence dependence of relaxation through a discussion of the Motional Averaging Regime and the Static Dephasing Regime.

In the third part of this work, we present results of *in vivo* experiments. Six-week-old male mice were orthotopically inoculated with GBM cells, and had been imaged over 22 days by the relevant pulse sequences. We then evaluate the model along with its implications by comparing results from simulations and experiments.

2.3 METHODS

2.3.1 Early brain tumor model

Transverse magnetizations of diffusing protons diphase due to local field inhomogeneity induced by paramagnetic deoxyhemoglobin inside blood vessels. Similar to the simulation in [7], our early stage tumor model where diffusion takes place consists of a voxel cube and inside it distributed with parallel infinite cylinders representing blood vessels. The total volume of cylinders is kept constant and the cube volume is obtained from the blood volume fraction (BVf). From [2], BVf is taken as 0.04 and vessel radius R to be $\frac{9\cdot10^{-6}}{\sqrt{N}}$ m to mimic early tumor environment for the RG2 model, where N is the number of vessels distributed inside the voxel cube. Each infinite vessel cylinder contributes an induced dipolar field ω_B as a component along the direction of the applied magnetic field B_0 [1]:

$$\omega_B = \begin{cases} 2\pi\Delta\chi(1-Y)\frac{B_0}{\gamma}\sin^2(\theta)\left(\frac{R}{r}\right)^2\cos(2\varphi), & r > R \\ 2\pi\Delta\chi(1-Y)\frac{B_0}{\gamma}\left(\cos^2(\theta)-\frac{1}{3}\right), & r < R \end{cases} \quad (1)$$

where γ is the proton gyromagnetic ratio, $(1-Y)$ is the degree of deoxygenation of the blood and was taken as 0.3 [2], θ is the angle between cylinder orientation and B_0, R is the vessel radius, r is the shortest distance to the vessel center of interest, φ is the angle between $\bar{r}$ and the projection of the main magnetic field onto the plane perpendicular to the vessel orientation, and $\Delta\chi$, the susceptibility difference between entirely deoxygenated blood and entirely oxygenated blood, assumes the value of 0.15 ppm [5].

2.3.2 Monte Carlo simulation

To ensure the validity of simulations, two different methods were implemented to evolve magnetizations under SE and CPMG pulse sequence. Initially 4000 spin magnetizations are randomly distributed inside the cube for method 1 and on a plane perpendicular to the vessels for method 2. During random walk, each step is taken as a random vector on a sphere for method 1 or on a circle for method 2 with step size obtained from three-dimensional [8] or two-dimensional diffusions, respectively. The diffusion constant D is taken as $1 \cdot 10^{-5}$ cm^2 s^{-1} [6] and time step Δt is taken as 0.05 ms. Small time steps make it impossible to traverse cylinders in a few steps. The cylinders are assumed to be impermeable for diffusion, while its impact on BOLD signal is very limited [9]. Steps that penetrate cylinders are repeated until a collision-free step is generated. By assuming the spatial periodicity of voxels, magnetizations that walk out of the voxel re-enters from the opposite side. To study the impact of aggregation of vessels, simulations are repeated with uniform distributions of 1, 2, 4 and 9 cylinders. Simulation results are averaged over 16 θ angles between 0 and π. All simulations are implemented using Matlab (*The Mathworks Inc*.).

2.3.3 Analytical method (Method 1)

The Bloch equation describes the classical dynamics of nuclear magnetizations. Via a complete analytical solution of the Bloch equation [10], exact evolution of magnetizations for each step during diffusion can be obtained by applying the propagator:

$$e^{-\Gamma\Delta t} = e^{-\bar{R}\Delta t}e^{-\Gamma_P\Delta t} \qquad (2)$$

where $-\Gamma$ is the Bloch equation in matrix form including T_2 terms, t is the time for each step, $\bar{R} = \frac{2}{3T_2}$ and $e^{-\Gamma_P t}$ is diagonalized. Denote the direction of B_0 as the z-direction. For SE pulse, the sign of magnetizations along x- and z-directions is inverted at TE/2. For CPMG pulse, the sign of magnetizations along x- and z- directions is inverted at $\tau_{cp}, 3\tau_{cp}, 5\tau_{cp}, \ldots$, where $\tau_{cp} = 8$ ms. For spin-locking pulse, a constant locking field of frequency 125 Hz is applied in the y-direction.

2.3.4 Phase accumulation method (Method 2)

The phase accumulation method was followed previous works [1, 11, 12] with additional modification of background relaxation. Base on the theory, at each time step, dt, every spin will experience different induced magnetic field which depends on its position (p) and undergoes a phase shift, $\Delta\phi(p) = \Delta\omega(p)*dt$. The overall phase shift for one spin can be achieved by summing up individual phase which produced by each step of random walk over time

$$\Phi = \sum_{n=1}^{step} \Delta\varphi(p_n) \qquad (3)$$

The accumulated phase gives the information, as the rotation of spin in the complex plane. With additional phase factor, $e^{i\varphi}$ or $\cos(\varphi)$, the "signal" of the magnetization can be determined

$$S(\theta) \approx \left|\frac{\sum_{j=spin} e^{i\Phi_j(\theta)}}{\sum_{j=spin} e^{i\Phi_0}}\right| = \left|\frac{\sum_{j=spin} s_j(\theta)}{\sum_{j=spin} s_0}\right| = \left|< s_j(\theta) >\right| \quad (4)$$

Note that in here, the signal is calculated by the ratio of the signals, s, with and without phase dispersion. Where s denotes the signal produced by individual spin, and φ_0 denotes the phase without phase dispersion. (We assumed $\varphi_0 = 0$ here.) Furthermore, since the magnetic fields follows linear superposition, the ensemble signal, S, which produced by total spin is simply the expectation value of the signal. The additional weighting factor of $\sin(\theta)$ and the flipping sign of phase for different pulse sequences are identical to previous method and not shown in here.

In addition, the signal decay here is calculated based on the average of constructive and destructive interference produced by the phase dispersion under the assumption of uniform amplitude of the signals. Therefore, the decay rate due to transverse relaxation, $R_{2,\,simulated}$, can be estimated as an exponential fitting with different values of TE.

$$S_{voxel}(TE) \approx \exp(-R_{2,simulated} * TE) \quad (5)$$

The phase accumulation method assumed all of the magnetizations are on xy plane, and the precession frequency is depended on the homogeneous B_0 magnetic field particularly. Therefore, the perturb field, B_1 field, cannot be included in this method.

2.3.5 Numerical Method

Method 3 uses the Bloch equation and the evolution of magnetization at each time point is solved by ordinary differential equation with the Matlab ode45 solver. This method is used to check the convergence with method 1.

2.3.6 In vivo experiments

Six-week-old male NOD CB17-Prkd^{scid}/IcrCr1B1tw (NOD/SCID) mice were obtained from BioLASCO Experimental Animal Center (BioLASCO, Taiwan) and bred in a specific pathogen-free room in the animal facility. All animal procedures were in accordance with the regulations approved by the Institution Animal Care and Utilization Committee at National Taiwan University. All operations were performed under anesthesia and any possible effort has been made to minimize pains/suffering of the mouse. For tumor implantation, each NOD/SCID mouse was anesthetized with Ketalar (40 mg/kg) and Rompun (15 mg/kg) and placed in a stereotactic frame for accurate location of implantation. The mice were orthotopically inoculated with GBM cells (5×10^5 cells per mouse) and used for MR imaging [13]. During the imaging acquisition, vital signs of the mouse under anesthesia (about 5% isoflurane induction, 2% for maintenance in air) was monitored. The flow rate of isoflurane was carefully adjusted to maintain stable heart rate and respiratory rate.

In this work, all in vivo experiments were performed on a Varian INOVA 7-T NMR spectrometer (Varian Inc., USA) equipped with a 30-mm I.D. Varian Millipede micro-imaging probe and self-shielded gradient systems with a maximum strength of 100 G cm^{-1} in each direction (Resonance Research Inc., USA). Images were acquired with

repetition time (TR) = 7.5 s, field of view (FOV) = 2.56 cm × 2.56 cm, matrix size = 128 × 128, zero padding = 512 × 512, and slice thickness = 0.8 mm. For spin echo pulse sequence, echo time (TE) = 10, 30, 50, 70, 90 ms. For CPMG pulse sequence, τ_{CP} = 8 ms (τ_{CP} is half the interval between successive 180^{o} pulses in a CPMG sequence, τ_{CP} = TE/2). For spin locking pulse sequence, locking field B_1 = 125 Hz.

2.4 RESULTS

2.4.1 Validation of simulation methods

Figure 1 plots the T_2 versus different field distributions with constant BVf and details the parameters used. Background T_2 parameters in the Bloch equation are chosen by comparing with experimental results from Figure 3. The results from method one and method two for simulating SE and CPMG pulses and method one and method three for simulating SL converge to within 1.5%. Agreement between different methods indicates that simulations are consistent in this model.

2.4.2 Vessel density dependence

The relation between cylinder density and relaxation rate is summarized in Figure 2. The figures below the axis of cylinders are the corresponding magnetic field perturbations. Cylinders are distributed such that the distance between nearest pairs remains constant across voxels when aligned periodically. Vessel radius varies with the number of cylinders from $9*10^{-6}$ m (max at 4 micrometer) to 3*10^-6 m to maintain BVf.

Signals decay faster for all pulse sequences across distributions of cylinders. Accounts of the Static Dephasing Regime (SDR) and the Motional Averaging Regime (MAR) provide an explanation for this trend. The change in T_2 relaxation per cylinder, $\frac{\Delta T_2}{\Delta C}$, decreases as the density of cylinder increases for all pulse sequences, where ΔC is the change in the number of cylinders. This diminution in the effect of density variation can be attributed to the decreasing difference in cylinder radius as discussed in Boxerman *et al.* [9].

2.4.3 Pulse sequence dependence (include T_2* values in the caption of Fig. 1)

To compare the effect of diffusion under different pulse sequences, background relaxations are set to infinity and the resulting diffusion relaxation constants T_2* are collected in Figure 1. The ensemble dephases the slowest with SL and the fastest with SE. Frequent refocusing in CPMG and SL delays decoherence from diffusion and longer T_2* results.

2.4.4 Comparison of model with in vivo data

Experimental MRI image and T_2 values for injected mouse models are plotted in Figures 3 and 4, respectively. From inspection of the two figures, we can see that no contrast is shown for SE at the early stage, while contrast is clear for the other two pulse sequences. T_2 values of the two tissues overlap for SE at the early stage. This can be reasoned as the effect of rephasing pulses on the two tissue environments described by our model. Since we cannot distinguish the two tissues under SE at the early stage, T_2 values from the other two pulse sequences are compared with simulations. From Figure 4, the simulation results match the experimental ones in that the normal tissue signals decay faster than the tumor ones. After 15 days, contrasts are enhanced greatly for all pulse sequences as edema evolves and the brain magnetic environment gets drastically different.

2.5 DISCUSSION

Most of the current papers on BOLD signal in the literature focus on improving the model, and yet, few of them describe the relationship with realistic early tumor relaxation. In the current approach by varying vessel densities/distributions, the resulting difference in T_2* between 1 and 9 cylinders can be ascribed to the competition between SDR and MAR. Furthermore, the difference in T_2* under different pulse sequences can be explained by the rephasing effect.

2.5.1 Vessel density dependence

From theories in [14], the Static Dephasing Regime is originally described as the limiting case where a particle with large interparticle distance compared to the diffusion distance experience nearly constant induced magnetic field during diffusion. Subsequently, the resulting relaxation rate will not be affected by the random walk of particles and will approach a static limit. On the other extreme, the Motional Averaging Regime is described as the limit that relatively small particles travel longer distance compare to the inter-particle distance and experience a rapid change in induced magnetic field. The resulting relaxation rate depends on the trajectory of each spin under random walk. Here, we extend these two regimes and assume identical particle size inside the voxel. As shown in Figure 1, the strength of induced inhomogeneous magnetic field is based on proton positions, and the largest dipolar field gradient is induced around the cylinders where the sign changes. In 1-cylinder case where the radius is largest, protons would need on average diffuse the most steps in order to experience large gradient. This

is similar to the case of SDR, and the resulting R_2* will be the smallest. For the 9-cylinder case, the dipolar field gradient changes more frequently around each cylinder, and protons will only need to diffuse few steps to experience a significant change in field, which is more adequately described by the MAR. In our simulation result, different distributions of vessels that span the two limiting regimes contribute major discrepancies between our tumor and healthy tissue models.

2.5.2 Rephasing effect of pulse sequences

Experimental results from Figure 2 show that CPMG and SL produce larger contrasts than SE between early tumor and healthy tissues. Our model can explain this effect via rephasing of magnetizations under different pulses. During diffusion, protons experience magnetic field gradient, which in turn dephase the ensemble by letting nuclei to precess at different rates. Hence the longer the time magnetizations can freely evolve under a varying field, the more decoherence occurs. When the ensemble magnetization is refocused by pi-y pulses, the phases are reversed back in time by reversing the order of fast and slow components, and decoherence is diminished along this process. Comparing to the difference between late stage tumor and normal tissue environments, the difference between different cylinder distributions in our model of early tumor and normal tissue environment is quite small. By this small variation of field environment described by our model, ensembles in early tumor and normal tissues gain similar decoherence after a large number of steps in diffusion.

Refocusing occurs at TE/2 for SE. This duration is so long such that the ensemble dephases to a comparable extent for 1 and 9 cylinder fields. As a result, signals for both fields cannot differentiate from each other after refocusing. For CPMG, however, the duration time, τ, between rephasing pulses is 16 ms which is significantly shorter than SE. In 1-cylinder environment, the induced field is essentially constant when diffusing only a few steps in the short tau and the ensemble can regain coherence after the refocusing pulse. For 9-cylinders where field gradient changes significantly within a few steps, and the effect is that magnetizations cannot restore to their original states. Therefore, larger contrast is produced for CPMG. An analogy can be established between CPMG and SL in that SL operates with consecutive rephasing pulses at an even shorter tau in this experiment. The frequent refocusing in SL makes the difference in field distributions most pronounced and in turn generates the best contrast.

2.5.3 Validation of the model

The effects of vascular permeability, volume fraction dependency, susceptibility difference are too small in the early stage brain tumor compared to normal tissue and are assumed to be negligible in our model. Truly, vessel network orientations may take significant role on induced magnetic field; however, the effect can be minimized by taking the advantage of small voxel-size compared to Martindale *et al.* [11]. As described earlier, we study the dependency of vascular size and density, and simulations exhibit the correct trend in relaxation rates. Note that our experimental settings are not applicable for imaging tumor tissue in human body due to the high power B_0 field and π

pulses applied, and it is not the purpose of this study. With this high field setting, the contrast can be easily established in the in-vivo imaging, Figure 3. As shown in Figure 2, the results from three different kinds of methods converge, and all of them produce the same trend, in which the 9-cylinder has higher relaxation rates than 1-cylinder due to the relative motional-average and static dephasing regime on the induced magnetic fields. We have also shown that the perturbing B_1 field constrain in SL and rapid rephasing of magnetizations in CPMG decrease the relaxation rate, yet increase the contrast between models. Hence, our research provides a clear track with fMRI sequence and early tumor model, and the result will be used and enhanced by later research with active feedback magnetic resonance.

2.6 CONCLUSION

In conclusion, a model of early brain tumor based on the BOLD mechanism is developed from the varying vessel densities that were observed experimentally. The model was illustrated using parameters typical for the early tumor environment [2-6] via three different approaches, producing results whose trends are consistent with experiments and are reasoned as a competition between two diffusing regimes. In addition, this model can be applied to explain the contrast difference between early stage and later stage tumor for the different pulse sequences. Finally, this model can be further revised by implementing features such as realistic distributions of vessel cylinder radius and orientations that were developed in Martindale *et al.* [11] to study the role of varying vessel densities in early stage brain tumor.

2.7 REFERENCES

[1] Ogawa S, Menon RS, Tank DW, Kim SG, Merkle H, Ellermann JM, Ugurbil K. Functional brain mapping by blood oxygenation level-dependent contrast magnetic resonance imaging. A comparison of signal characteristics with a biophysical model. Biophys J 1993; 64(3): 803-812.

[2] Valable S, Lemasson B, Farion R, Beaumont M, Segebarth C, Remy C, Barbier EL. Assessment of blood volume, vessel size, and the expression of angiogenic factors in two rat glioma models: a longitudinal in vivo and ex vivo study. NMR Biomed 2008; 21: 1043-1056.

[3] Christen T, Lemasson B, Pannetier N, Farion R, Remy C, Zaharchuk G, Barbier EL. Is $T2^*$ enough to assess oxygenation? Quantitative blood oxygen level-dependent analysis in brain tumor. Radiology 2012; 262: 495-502.

[4] Yao J, Maslov KI, Zhang Y, Xia Y, Wang LV. Label-free oxygen-metabolic photoacoustic microscopy in vivo. J Biomed Optics 2011; 16(7): 076003.

[5] Boxerman JL, Hamberg LM, Rosen BR, Weisskoff RM. MR contrast due to intravascular magnetic susceptibility perturbations. Magn Reson Med 1995; 34: 555-566.

[6] Chien D, Buxton RB, Kwong KK, Brady TJ, Rosen BR. MR diffusion imaging of the human brain. J Comput Assist Tomogr 1990; 14(4): 514-520.

[7] Dickson JD, Ash TW, Williams GB, Harding SG, Carpenter TA, Menon DK, Ansorge RE. Quantitative BOLD: the effect of diffusion. J Magn Reson Imaging 2010; 32(4):953-961.

[8] Li Z, Hsu C, Dimitrov N, Hwang DW, Chang H, Hwang L, Lin, Y. Sensitive Imaging of Magnetic Nanoparticles for Cancer Detection by Active Feedback MR. Magn Reson Med 2015; 74: 33-41.

[9] Boxerman JL, Bandettini PA, Kwong KK, Baker JR, Davis TL, Rosen BR, Weisskoff RM. The intravascular contribution to fMRI signal change: Monte Carlo modeling and diffusion-weighted studies in vivo. Magn Reson Med 1995; 34(1): 4-10.

[10] arXiv:1704.00826 [quant-ph]

[11] Martindale J, Kennerley AJ, Johnston D, Zheng Y, Mayhew JE. Theory and generalization of Monte Carlo models of the BOLD signal source. Magn Reson Med 2008; 59: 607-618.

[12] Dickson JD, Ash TW, Williams GB, Sukstanskii AL, Ansorge RE, Yablonskiy DA. Quantitative phenomenological model of the BOLD contrast mechanism. J Magn Reson 2011; 212: 17-25.

[13] Yao J, Hsu C, Li Z, Kim TS, Hwang L, Lin Y, Lin, Y. Magnetic Resonance Nano-Theranostics for Glioblastoma Multiforme. Curr Pharm Des 2015; 21: 5256-5266.

[14] de Haan HW. Mechanisms of proton spin dephasing in a system of magnetic particles. Magn Reson Med 2011; 66(6): 1748-1758.

2.8 FIGURES

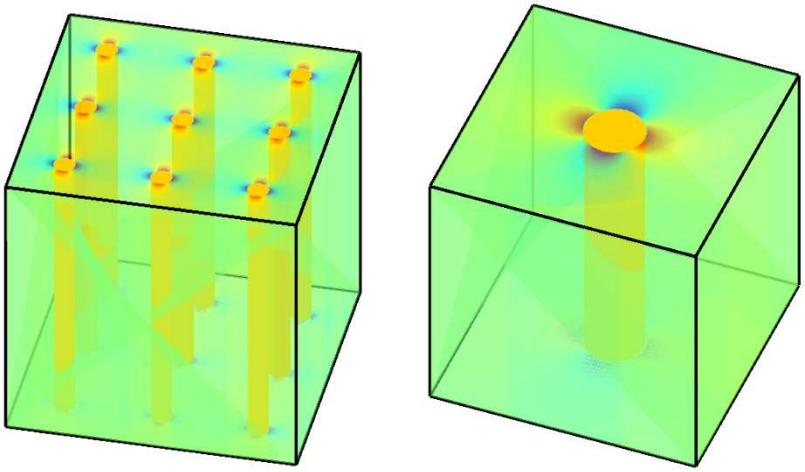

Figure 1. Z-component of the magnetic field generated by 9-cylinders (left) and 1-cylinder (right) with the same blood volume fraction of BVf = 0.04.

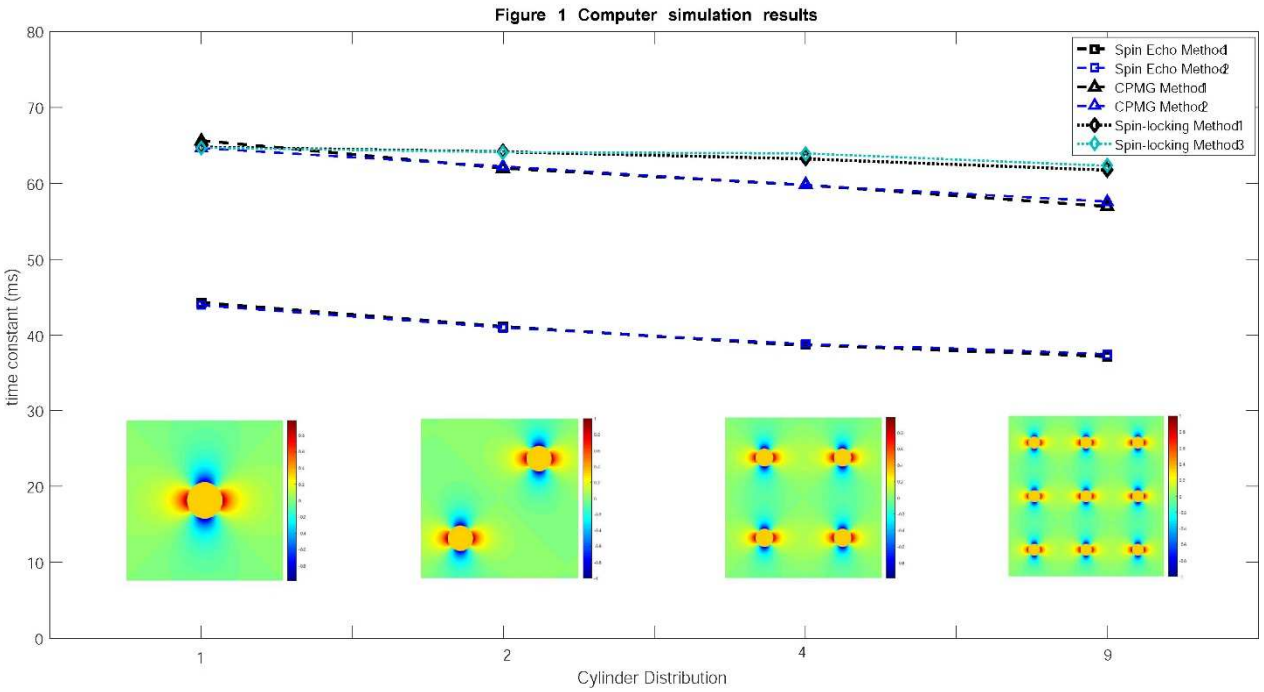

Figure 2. Time constants of the three pulse sequences (spin echo, CPMG, and spin locking) for various field distributions (1-cylinder, 2-cylinders, 4-cylinders, and 9-cylinders) with constant BVf. For each pulse sequence, two simulation methods were used and the results from the two methods converged. The background relaxation parameters used for spin echo, CPMG, and spin locking are 55ms, 70ms, and 65ms, respectively.

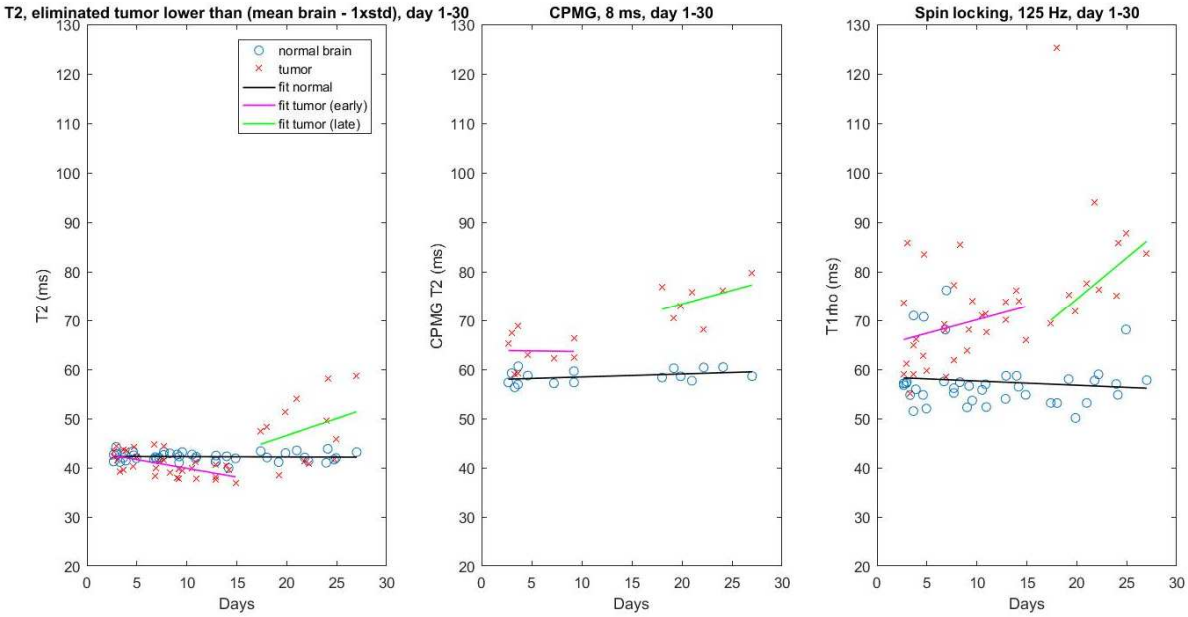

Figure 3. Time constants of normal brain (averaged from left brain tissue) and tumor of spin echo (TE = 30 ms), CPMG (τ_{CP} = 8 ms), and spin locking (B_1 = 125 Hz) pulse sequences, acquired from 1 day to 30 days after implantation of GBM cells to the right brain of mouse. The linear regression of normal brain time constant (in ms): $T_{2,\ SE}^{brain} = -5.47 \times 10^{-3} \times days + 42.30$, $T_{2,\ CPMG}^{brain} = 6.12 \times 10^{-2} \times days + 57.85$, $T_{1\rho}^{brain} = -8.62 \times 10^{-2} \times days + 58.50$. The linear regression of tumor time constant (in ms) at early stage (within 15 days after implantation): $T_{2,\ SE}^{brain} = -0.35 \times days + 43.41$, $T_{2,\ CPMG}^{brain} = -0.025 \times days + 63.89$, $T_{1\rho}^{brain} = 0.55 \times days + 64.60$. The linear regression of tumor time constant (in ms) at late stage (after 15 days after implantation): $T_{2,\ SE}^{brain} = 0.69 \times days + 32.77$, $T_{2,\ CPMG}^{brain} = 0.56 \times days + 62.28$, $T_{1\rho}^{brain} = 1.68 \times days + 40.80$.

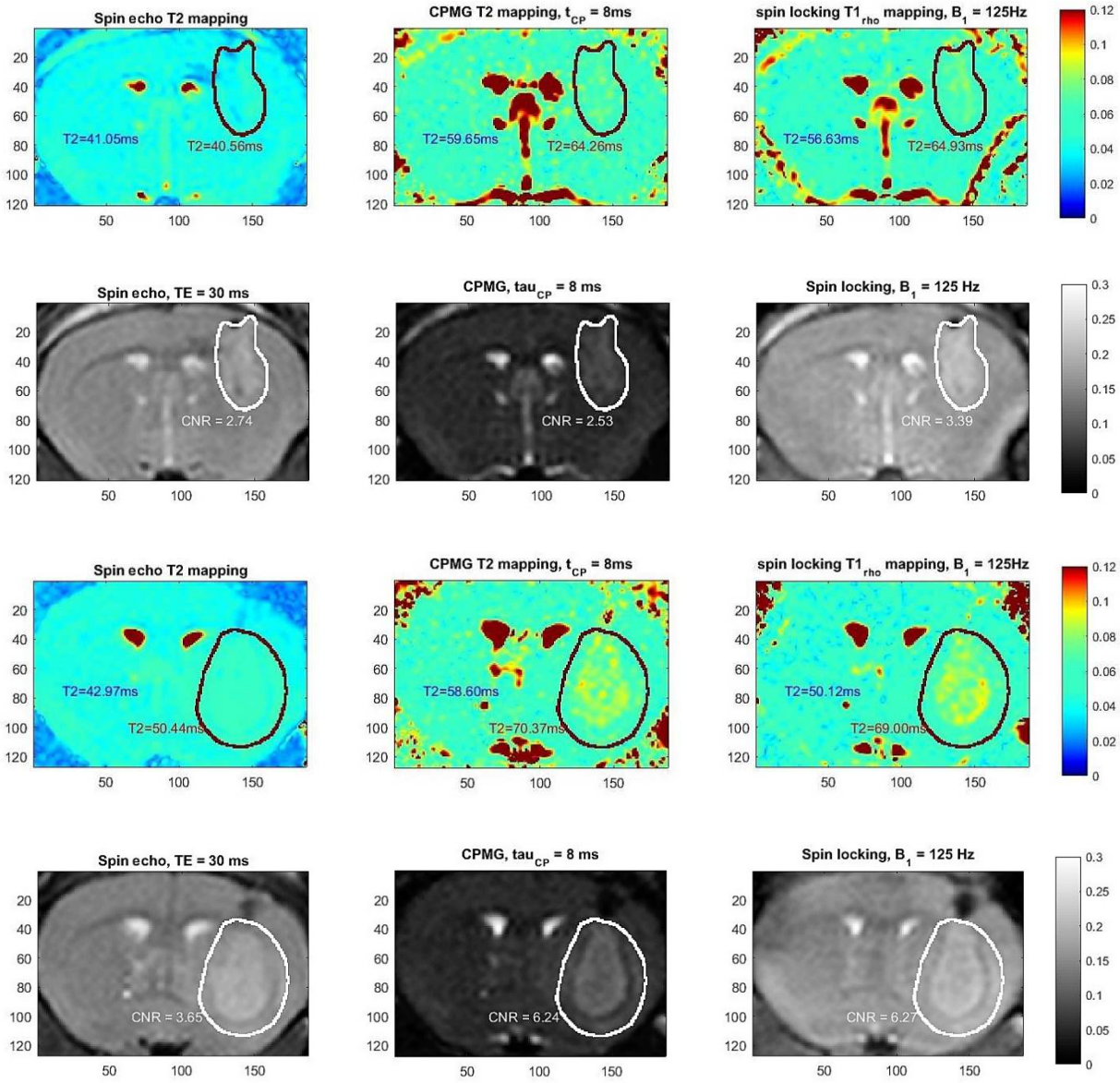
Spin echo T2 mapping
T2=41.05ms
T2=40.56ms
CPMG T2 mapping, t_CP = 8ms
T2=59.65ms
T2=64.26ms
spin locking T1_rho mapping, B_1 = 125Hz
T2=56.63ms
T2=64.93ms
Spin echo, TE = 30 ms
CNR = 2.74
CPMG, tau_CP = 8 ms
CNR = 2.53
Spin locking, B_1 = 125 Hz
CNR = 3.39
Spin echo T2 mapping
T2=42.97ms
T2=50.44ms
CPMG T2 mapping, t_CP = 8ms
T2=58.60ms
T2=70.37ms
spin locking T1_rho mapping, B_1 = 125Hz
T2=50.12ms
T2=69.00ms
Spin echo, TE = 30 ms
CNR = 3.65
CPMG, tau_CP = 8 ms
CNR = 6.24
Spin locking, B_1 = 125 Hz
CNR = 6.27

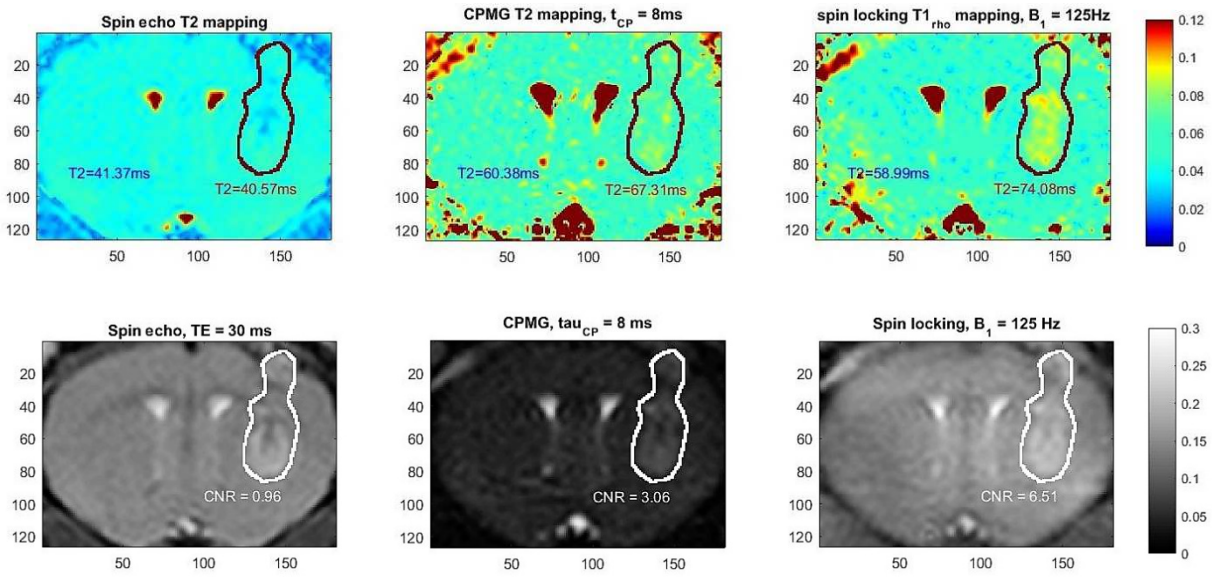

Figure 4. Development of GBM contrast in orthotopic U87MG mouse models during its clinical course acquired by spin echo (TE = 30 ms), CPMG (τ_{CP} = 8 ms), and spin locking (B_1 = 125 Hz) pulse sequences. Average time constants values of normal left brain tissue and tumor, respectively, are given in the time constant mappings. Contrast-to-noise ratios (CNR) for each pulse sequence is directly given on each image. At both early stage (within 15 days after implantation) and late stage (after 15 days after implantation), CPMG and spin locking show superior contrast than spin echo. At late stage, the metabolic by-products from the GBM cells' mitosis and growth increase the local osmotic gradient of the extracellular fluid. This results in the ingress of fluid from the intravascular space to increase the T_2 time constant to make GBM detectable in the spin echo T_2-weighted images.

CHAPTER 3

Quantum Fixed-Point Spin Dynamics by Active Feedback Magnetic Resonance for Early Cancer Imaging

*This work is contributed by Chao-Hsiung Hsu, Jon K. Furuyama, Zhao Li, Jamie D. Walls, Chencai Wang, Lian-Pin Hwang and Yung-Ya Lin. (Shang-Lin Tsai, Guan Wang verified and revised this work)

3.1 ABSTRACT

The use of weak continuous wave (CW) irradiation in the presence of passive or active feedback fields is shown to produce unique stable fixed points (or constants of motion). The location of the fixed points as well as the quantum dynamics en route to the fixed points are investigated within a density operator framework. Applications for imaging contrast enhancement for early brain tumor detection are discussed and demonstrated.

3.2 INTRODUCTION

With regards to biomedical diagnostics, magnetic resonance imaging (MRI) has a great advantage due to its employment of low-energy, non-ionizing radio-frequency (RF) radiation [1]. Unfortunately, this increase in safety and applicability comes at the expense of the immense specificity that is present in other imaging modalities that make use of ionizing radiation, such as Computed Tomography (CT) and Positron Emission Tomography (PET) [2]. Contrast in MRI is currently dependent on the molecular dynamics of differing tissues, resulting in variety of relaxation times of the signal. This can be very limiting when trying to differentiate between tissues or materials with only a slight difference in relaxation parameters, as is the case in trying to distinguish between early tumors and healthy tissue. The advent of early brain tumors can be marked by a slight shift in magnetic susceptibility. This meager shift in the local field is independent of molecular dynamics and is thus essentially invisible to the conventional, relaxation-based imaging mechanisms. There has thus been an interest in the development of robust imaging techniques that are sensitive to the local susceptibility variations across a sample [3–6].

In this work, it is shown that the use of weak continuous wave (CW) radiation in the presence of the passive or active feedback fields is sensitive to the small magnetic susceptibility differences of a sample, producing unique and fortuitous fixed-points on opposite sides of the Bloch sphere. The evolution of the magnetization en route to the fixed points was shown to be useful in the detection of early brain tumors in mice, having a much improved contrast-to-noise (CNR) ratio over conventional imaging methods. Here we lay forth a theoretical foundation for the development of the fixed points, and

analyze the quantum dynamics and how they can be useful for the development of imaging contrast.

The passive feedback field of radiation damping was discovered and characterized in the early days of NMR [7]. By Lenz's law, an induced oscillating current in a coil will be met by an opposing oscillating field. This reactionary field can then act back onto the sample, accelerating the magnetization back towards the equilibrium +z position, shortening the FID. The decreased signal lifetime thus corresponds to a significantly broadened solvent peak in the sample spectrum, obscuring important peaks, especially in high-field biomolecular NMR. Feedback fields can also be generated from homebuilt active feedback-controlled electronic device. The device is to filter, phase shift, and amplify the signal from the receiver coils and then retransmit the modified signal into the RF transmission coil, with adjustable and programmable feedback phases and gains. The MR console computer can execute the active-feedback pulse sequences to control the trigger signal, feedback phase/gain, and the duration of the feedback fields, allowing us to utilize the active feedback fields in novel ways. The inherent dependence of the feedback field on the instantaneous state of the sample causes the evolution of the magnetization to be nonlinear and even chaotic [8–10].

With the advent of pulsed Fourier NMR [11], the use of a CW in both spectroscopy and imaging has been reserved for secondary dynamics such as decoupling or presaturation [12]. In other experiments, a CW is used to tilt the effective field in order to study relaxation behaviors in different frames of reference [13]. The constant perturbation of the CW coupled with the non-linear evolution resulting from the passive or active feedback fields would thus not be expected to produce stable fixed-points of the

magnetization that are not at the equilibrium +z position. While the dynamics surrounding both a CW and passive/active feedback fields can be modeled classically [9, 10], the physical origin behind the fixed points is much more transparent within a density operator formalism. The following theory can thus be recast within the more familiar classical framework, but with less intuition and prediction as to the nature of the fixed points themselves.

3.3 METHODS AND RESULTS

The Hamiltonian for a spin system in the laboratory frame can be given by

$$\hat{H}_{lab}(t) = \hat{H}_0 + \hat{H}_1(t) \quad (1)$$

where $\hat{H}_0$ and $\hat{H}_1$ represent the static and interaction Hamiltonians, respectively. The static Hamiltonian is the familiar Zeeman interaction, $\hat{H}_0 = -\hbar\omega_0\hat{I}_z$, where $\omega_0 = -\gamma B_0$. The interaction Hamiltonian contains information regarding any resonance offset as well as the static excitation of the radio-frequency field

$$\hat{H}_I = \hbar\omega_1 \left(e^{-i\hat{I}_z\omega_0 t} \hat{I}_x e^{i\hat{I}_z\omega_0 t} \right) + \hbar\delta\omega\hat{I}_z \quad (2)$$

where $\hbar\delta\omega$ represents the resonance offset from the Larmor frequency ω_0. The Rabi frequency ω_1 [14] is proportional to the strength of the excitation field. The equation of motion for the density operator under a particular Hamiltonian is thus given by the Liouville-von Neumann equation:

$$\frac{\partial\hat{\rho}(t)}{\partial t} = -\frac{i}{\hbar}\left[\hat{H}_0 + \hat{H}_I, \hat{\rho}(t)\right] \quad (3)$$

By simple unitary transformation, using $\hat{U}(t) = e^{i\hat{I}_z\omega_0 t}$, Eq. 3 can be transformed to the Dirac picture (or rotating frame of reference at frequency ω_0) such that

$$\frac{\partial\hat{\rho}^*(t)}{\partial t} = -\frac{i}{\hbar}\left[\hat{H}_I^*, \hat{\rho}^*(t)\right] \quad (4)$$

Where $\hat{H}_I^* = \hbar\delta\omega\hat{I}_z + \hbar\omega_1\hat{I}_x$. For the sake of brevity, the asterisks and interaction subscripts are dropped as the rest of the discussion is within the Dirac picture.

For a two-component uncoupled system, the total Hamiltonian for both spins is simply the sum of the individual Hamiltonians, $\hat{H}_{ij} = \hat{H}_i + \hat{H}_j$, where the subscript notation refers to tensor operators corresponding to the ith and jth spins in the Liouville space. These two components differ only in their resonance offset such that $\Delta\omega_{ij} = \delta\omega_i - \delta\omega_j \neq 0$. For simplicity, assume that the offset for both components is equal in magnitude such that $\delta\omega_i = -\delta\omega_j = \delta\omega$. The interaction Hamiltonian for these two spins can thus be simplified to

$$\hat{H}_{ij} = \hbar\omega_1 \hat{I}_{x,ij} + \hbar\delta\omega \hat{I}_{z,ij} \quad (5)$$

where $\hat{I}_{x,ij} = \hat{I}_{x,i} + \hat{I}_{x,j}$, and $\hat{I}_{z,ij} = \hat{I}_{z,i} - \hat{I}_{z,j}$. While the time evolution of the system under this Hamiltonian is not of any particular interest, the constants of motion (or called "fixed points" of the dynamics) are worth investigating, as the results are somewhat surprising in the presence of feedback fields.

The constants of motion can be solved by simply setting Eq. 4 equal to zero. These can be seen to simply be the density matrices that commute with $\hat{H}_{ij}$. Since the Hamiltonian can be simply expanded as a vector in Liouville space, the constants of motion, $\hat{\rho}_{ij} = \hat{\rho}_i + \hat{\rho}_j$, where $\hat{\rho}_{i/j}$ are just the vectors that lie either parallel or anti-parallel to $\hat{H}_{i/j}$ and are obtained via an orthogonalization process illustrated in [15]. Refer to the supplementary material for detailed procedure. The four physically relevant constants of motion are thus

$$\begin{aligned}
\hat{\rho}_{++} &= \tfrac{1}{4}\hat{\mathbf{1}} + l\left(\hat{H}_i + \hat{H}_j\right) \\
\hat{\rho}_{+-} &= \tfrac{1}{4}\hat{\mathbf{1}} + l\left(\hat{H}_i - \hat{H}_j\right) \\
\hat{\rho}_{-+} &= \tfrac{1}{4}\hat{\mathbf{1}} - l\left(\hat{H}_i - \hat{H}_j\right) \\
\hat{\rho}_{--} &= \tfrac{1}{4}\hat{\mathbf{1}} - l\left(\hat{H}_i + \hat{H}_j\right)
\end{aligned} \quad (6)$$

where $l = \frac{\delta\omega}{\hbar\left(\delta\omega^2+\omega_1^2\right)}$, $\hat{\mathbf{1}}$ is the identity operator, and the ± subscript notation is used in reference to the sign in front of each respective Hamiltonian term. Physically, it can be seen that the $\rho\hat{}_{++}$ state has both components aligned with the effective field, with the $\rho\hat{}_{--}$ state with both components anti-parallel to the effective field. Likewise, both of the $\rho\hat{}_{+-}$ and $\rho\hat{}_{-+}$ states have one component aligned with the effective field, and one aligned anti-parallel. Energetically, since $E_{ij} = Tr[H\hat{}_{ij}\rho\hat{}_{ij}]$, it can be seen that the $\rho\hat{}_{++}$ state is lowest in energy and the $\rho\hat{}_{--}$ state being the highest in energy, with both the $\rho\hat{}_{+-}$ and $\rho\hat{}_{+-}$ states in between, as would be expected. In the event that the frequency difference between the two components is small, it would be near impossible to selectively excite one component over the other, making the $\rho\hat{}_{+-}$ and $\rho\hat{}_{-+}$ states practically inaccessible, and thus not very interesting. This is not the case, however, in the presence of feedback fields.

In order to analyze the constants of motion in the presence of feedback fields, a semi-classical coupling term needs to be added to Eq. 5 for each component of the form

$$\hat{H}_{FF,i} = \hbar\omega_r \left(\Re\left[\langle i\hat{I}_{ij}^{+}\rangle(t)\right]\hat{I}_{x,i} + \Im\left[\langle i\hat{I}_{ij}^{+}\rangle(t)\right]\hat{I}_{y,i}\right) \quad (7)$$

where ω_r is the strength of the passive/active feedback fields, $\Re$ and $\Im$ represent the real and imaginary component of $\langle iI_{ij}^{+}\rangle(t) = iTr[I\hat{}ij + \rho\hat{}ij(t)]$, and $I\hat{}_{ij}+ = p_iI\hat{}_i^{+} + p_jI\hat{}_j^{+}$ with $p_i + p_j = 1$, where $I\hat{}_{i/j}^{+}$ are the raising operators. In this particular case, $p_i = p_j = 1/2$. The imaginary number in Eq. 7 represents a complex rotation of $\langle iI_{ij}^{+}\rangle(t)$ such that the feedback fields is always applied 90 out of phase with total transverse magnetization, or that $H\hat{}_{FF} \perp \langle iI_{ij}^{+}\rangle(t)$. The total Hamiltonian, $H\hat{}'_{ij} = H\hat{}_{ij} + H\hat{}_{FF}$, for the sample thus becomes

$$\hat{H}'_{ij} = \hbar\delta\omega\hat{I}_{z,ij} + \left(\hbar\omega_r\Re\left[\langle i\hat{I}_{ij}^{+}\rangle(t)\right] + \hbar\omega_1\right)\hat{I}_{x,ij} + \hbar\omega_r\Im\left[\langle i\hat{I}_{ij}^{+}\rangle(t)\right]\hat{I}_{y,ij} \quad (8)$$

where $\hat{I}_{y,ij} = \hat{I}_{y,i} + \hat{I}_{y,j}$. It can be seen that the functional form of Eq. 7 contains pseudo-bilinear terms such as $\langle I_{ij}^{+} \rangle \hat{I}_{x,i}$, which differ significantly from the familiar two-spin coupling terms, but nonetheless represent a coupling of each spin with the rest of the sample.

From Eq. 6, it can be seen that since the constants of motion align either parallel or anti-parallel to the uncoupled Hamiltonian, then $\langle I_{ij}^{+} \rangle \parallel \hat{H}_{ij} \perp \hat{H}_{FF}$. Thus $[\hat{H}_{ij}, \hat{H}_{FF}] \neq 0$ unless $\hat{H}_{FF} = 0$, which can only be the case when $\langle I_{ij}^{+} \rangle = 0$. For both of the $\hat{\rho}_{++}$ and $\hat{\rho}_{--}$ states, it can be seen that $\langle I_{\pm\pm}^{+} \rangle = Tr\left[I_{ij}^{+} \rho_{\pm\pm}\right] \propto \pm\omega_I \neq 0$, and so $[\hat{H}_{ij}', \hat{\rho}_{\pm\pm}] \neq 0$ meaning that both the $\hat{\rho}_{++}$ and $\hat{\rho}_{--}$ states are annihilated as constants of motion with the addition of feedback fields. This is not the case, however, with the $\hat{\rho}_{+-}$ and $\hat{\rho}_{-+}$ states, where it can be seen that $\langle I_{\pm\mp}^{+} \rangle = 0$ because both components are anti-parallel to each other, and so $\hat{H}_{FF} = 0$. Consequently, $\hat{H}_{ij} = \hat{H}_{ij}'$, and thus both of the anti-parallel states are preserved as constants of motion, since they already commute with the uncoupled Hamiltonian.

Thermodynamically, the $\hat{\rho}_{+-}$ and $\hat{\rho}_{-+}$ states are energetically favored over the $\hat{\rho}_{++}$ and $\hat{\rho}_{--}$ states, which are no longer constants of motion. From Eq. 7, it can be seen that for $\langle I_{ij}^{+} \rangle = 0$, the feedback-field term is going to be in direct competition with the uncoupled interaction Hamiltonian since they are applied perpendicular to each other. As the feedback-field term becomes larger, it begins to draw each component away from the uncoupled Hamiltonian, subsequently raising the total Zeeman energy of the system. Consequently, the system will naturally adopt the configuration that can minimize $\langle I_{ij}^{+} \rangle$, thus reducing $\hat{H}_{FF}$. When $\Delta p_{ij} = |p_i - p_j| = 0$, it is easy to see that the components can

align to perfectly cancel each other out such that $\langle I_{ij}^{+} \rangle = 0$, and thus $\hat{H}_{FF} = 0$. In the event that each component does not have equal contribution to the feedback fields, $\Delta p_{ij} \neq 0$, and so $\hat{H}_{FF} \neq 0$. Since $\hat{H}_{FF} \perp \hat{H}_{ij}$, the total energy for both the ρ'_{+-} and $\hat{\rho}'_{-+}$ states raises because these states are no longer aligned with the total field.

The degree in which the $\hat{\rho}'_{+-}$ and $\hat{\rho}'_{-+}$ states shift can be quite challenging to determine analytically. One method could be to treat $\hat{H}_{ij}' = \hat{H}_{ij} + \hat{H}_{FF}$ in a perturbative sense where $\hat{H}_{ij}$ is the unperturbed Hamiltonian for which we have the constants of motion, and $\hat{H}_{FF}$ is the perturbation for which the corrections can be solved for. This approach is significantly complicated by the fact that the perturbation is dependent on many factors, including the density matrix itself. Understandably, any non-zero feedback fields will tilt $\hat{\rho}'_{+-}$ and $\hat{\rho}'_{-+}$ away from the original axis in order to minimize the total energy. However, in doing so, the direction of the feedback fields will then change requiring $\hat{\rho}'_{+-}$ and $\hat{\rho}'_{-+}$ to tip away even further from the original axis. Eventually, the amount of energy that the system can gain from tipping $\hat{\rho}'_{+-}$ and $\hat{\rho}'_{-+}$ will be balanced out by the energy cost of rotating $\hat{\rho}'_{+-}$ and $\hat{\rho}'_{-+}$ away from the static field, $\omega_1 \hat{I}_x$. Additionally, in order to minimize $\langle I_{ij}^{+} \rangle$, the system could tip both components away from the transverse plane. Again, this comes at the cost of tipping the components away from $\omega_1 \hat{I}_x$, which raises the total energy of the system. Thus, there is a direct competition between the resonance offset, $\delta\omega$, the excitation field, ω_1, and the feedback field, $\hat{H}_{FF} \propto \Delta p_{ij} \omega_r$. The orientations of $\hat{\rho}'_{+-}$ and $\hat{\rho}'_{-+}$ that minimize the energy can thus be determined using a variational approach.

By setting $\sqrt{\omega_1^2 + (\Delta p_{ij} \omega_r)^2} \gg \delta\omega$, an approximation can be made for how much $\hat{\rho}'_{+-}$ and $\hat{\rho}'_{-+}$ need to shift in order to minimize the total energy. This constraint ensures

that the reorientation of $\rho\hat{}'_{+-}$ and $\rho\hat{}'_{-+}$ be dominated by the interplay between ω_1 and $\Delta p_{ij}\omega_r$. The constraint is reasonable because the origin of the fixed points is a direct consequence of mixing the excitation field and the feedback fields, and less dependent on the magnitude of the actual resonance offset of each component. Considering that the total energy is minimized when $\langle I_{ij}^{+}\rangle \parallel (H\hat{}_{ij} + H\hat{}_{FF})$ along with the fact that $\langle I_{ij}^{+}\rangle \perp H\hat{}_{FF}$, by simple geometric argument one can show that the angle, θ_t, both $\rho\hat{}'_{+-}$ and $\rho\hat{}'_{-+}$ need to be rotated to minimize the energy can be given as

$$\theta_t \cong \tan^{-1}\left[\frac{\Delta p_{ij}\omega_r \cos(\theta_t)}{\omega_1 - \Delta p_{ij}\omega_r \sin(\theta_t)}\right] = \sin^{-1}\left[\frac{\Delta p_{ij}\omega_r}{\omega_1}\right] \tag{9}$$

where this can be seen to only be valid for $\omega_1 \geq \Delta p_{ij}\omega_r$. It can thus be seen that when both components do not contribute equally to the feedback fields, the $\rho\hat{}'_{+-}$ and $\rho\hat{}'_{-+}$ states become

$$\rho\hat{}'_{\pm\mp} \cong e^{i\Gamma z\theta t}\rho\hat{}_{\pm\mp}\, e^{-i\Gamma z\theta t} \tag{10}$$

where $I\hat{}_z = I\hat{}z_{,i} + I\hat{}z_{,j}$. In the limit that either $\Delta p_{ij} \rightarrow 0$ or $\omega_r \rightarrow 0$, the orientations of the $\rho\hat{}'_{+-}$ and $\rho\hat{}'_{-+}$ states converge to the original $\rho\hat{}_{+-}$ and $\rho\hat{}_{-+}$ states as expected. While the anti-parallel orientations of the $\rho\hat{}_{+-}$ *and* $\rho\hat{}_{-+}$ states originate from minimizing the total energy of the system, the development of these fixed-points from equilibrium is not trivial and requires a more in-depth analysis.

At equilibrium, the density matrix is given by

$$\hat{\rho}_0 = \frac{1}{4}\hat{\mathbf{1}} + \frac{\mathbf{P}}{4}\left(\hat{I}_{z,i} + \hat{I}_{z,j}\right) \tag{11}$$

where $\boldsymbol{P} = \tanh(\hbar\gamma B_0/k_B T)$. Evolution of the density matrix in the appropriate frame of reference is governed by the Liouville-von Neumann equation as given in Eq. 4. In the absence of feedback fields, the solution to Eq. 4 for the Hamiltonian given in Eq. 5 is simply

$$\hat{\rho}(t) = \underline{\widehat{U}_{ij}}(t)\hat{\rho}_0 \quad (12)$$

where $\underline{\widehat{U}_{ij}}$ is just the super operator ($\underline{\widehat{U}_{ij}}$ A = $U_{ij}^{\wedge}\, A\, U_{ij}^{\wedge -1}$) form of

$$U_{ij}(t) = exp\{iI'_{x,ij}\omega_e t\}\, exp\{iI_{y,ij}\theta_{i/j}\} \quad (13)$$

where $I^{\wedge}_{x,ij}{}' = exp\{iI^{\wedge}_{y,ij}\theta_{i/j}\}(I^{\wedge}_{x,ij})exp\{-iI^{\wedge}_{y,ij}\theta_{i/j}\}$ is a rotation of the excitation field by an angle $\theta_{i/j} = \tan^{-1}[\delta\omega_{i/j}/\omega_1]$, and the frequency of rotation about the new excitation axis is $\omega_e = (\omega_1^2 + \delta\omega_{i/j}^2)^{1/2}$. This solution is simply a rotation of each component around the effective field.

Solving Eq. 4 with the Hamiltonian in Eq. 8 is not trivial. As previously discussed, the Hamiltonian in Eq. 8 not only varies with time, but has an explicit dependence on the instantaneous state of $\rho^{\wedge}(t)$, rendering the time evolution as non-linear. The propagator, $\underline{U_{ij}}(\delta t, \hat{\rho}(t'))$, dependent on the density operator at time, t′, acts for a short interval, δt, such that the density operator at time t = t′ + δt can be given as

$$\begin{aligned}\hat{\rho}(t) &= \underline{\widehat{U}_{ij}}(\delta t, \hat{\rho}(t'))\, \hat{\rho}(t') \\ &= \underline{\widehat{U}_{ij}}(\delta t, \hat{\rho}(t'))\, \underline{\widehat{U}_{ij}}(\delta t, \hat{\rho}(t''))\, \hat{\rho}(t'') \\ &= \underline{\widehat{U}_{ij}}(\delta t, \hat{\rho}(t'))\, \ldots\, \underline{\widehat{U}_{ij}}(\delta t, \hat{\rho}(t_0))\, \hat{\rho}(t_0)\end{aligned} \quad (14)$$

where t′ = t″ + δt, until $t_{n-1} = t_0 + \delta t$. As seen in Eq. 7 and 8, any immediate change in $\rho^{\wedge}(t)$ is immediately reflected in a new Hamiltonian acting on $\rho^{\wedge}(t + \delta t)$. This calls for the limit where $\delta t \rightarrow 0$, requiring an infinite recursion of propagators from time $t_0 \rightarrow t$. This sort of

analytical consideration becomes intractable, considering the extreme sensitivity to initial conditions. An approximate solution for $\hat{\rho}(t)$ can be obtained by numerical integration of Eq. 4 using the Hamiltonian in Eq. 8 and initial conditions in Eq. 11. The result is shown in Fig. 1A. Starting from equilibrium, the expectation values for each component can be seen to spiral away from the other component, towards stable fixed points on opposite poles of the Bloch sphere. The location of these fixed points is consistent with the constants of motion presented in Eq. 6, and this particular orientation represents the $\hat{\rho}_{-+}$ state. Numerical analysis reveals that, while the $\hat{\rho}_{+-}$ state is fixed, it is not stable and thus can only be achieved if the system starts in this specific state. The development of these states is understandably a result of the competition between the excitation field, and the feedback fields.

In the absence of feedback fields, the effect the excitation field is to invert the populations of the density matrix on a time scale of $\tau = (2\omega_1)^{-1}$, or one half of the inverse Rabi frequency. The populations are then inverted a second time on the same time scale, bringing the density matrix back to $\hat{\rho}_0$. In the presence of feedback fields, a different time scale can be predicted because population inversion requires the creation of coherences, $\langle I_{ij}^{+} \rangle$, which activates Eq. 7. The net effect of Eq. 7 is to create an imbalanced Rabi cycle, where the feedback fields destructively interfere with the initial population inversion, requiring a time scale of $\tau_1 > (2\omega_1)^{-1}$, and constructively interferes with the second inversion, reducing the time scale to $\tau_2 < (2\omega_1)^{-1}$.

In the presence of the $\delta\omega_{i/j}\hat{I}_{z,i/j}$ terms, the $\langle I_{i/j}^{+} \rangle$ part of each component will acquire a phase during the initial inversion, and a negative phase during the second inversion of the populations. Without feedback fields, the required time to invert the

populations is equal, and so after one full cycle, the net acquired phase for each component is zero. In the presence of feedback fields, the time required for both inversions is different, and so it can be easily seen that the magnitude of the acquired phase during the first inversion will be greater than that of the second inversion, resulting in a net phase accumulation after one full cycle. In this example, since $\delta\omega_i = -\delta\omega_j$, it can be seen that there will be a net phase difference between both components after one full rotation. Subsequent inversion cycles allow for the process to repeat itself indefinitely until the total system arrives at its constant of motion, or fixed points.

The rate at which the system evolves towards the fixed points depends on the extent of the imbalanced Rabi cycle. Increasing ω_r with respect to ω_1 creates a larger imbalance, allowing for a greater phase accumulation between each component for a given cycle. Consequently, fewer cycles are required in order for each component to obtain a maximum phase separation. Conversely, reducing ω_r with respect to ω_1 decreases the imbalance, diminishing the total phase accumulation for each cycle, thus increasing the amount of time required to reach the fixed points, as can be seen in Fig. 1B. The time required to reach the fixed points is inversely proportional to the imbalance in the Rabi cycle. Of course, in the limit that $\omega_1 \gg \omega_r$, the imbalance becomes negligible, and there will be effectively no phase accumulation between each component. On the same note, in the limit that $\omega_1 \ll \omega_r$, the feedback fields prevent any possible inversion, hindering any phase accumulation. So it can be seen that the condition that $\omega_1 \sim \omega_r$ must be met in order for the constants of motion to develop on any reasonable time scale.

The development of the fixed points is rather straight forward in the case where $\Delta p_{ij} = 0$ because of the even symmetry between both components. There is a significant

shift in dynamics when the symmetry is broken ($\Delta p_{ij} \neq 0$) as can be seen in Figs. 2B-D. The effect of simply changing $p_i = p_j$ (2A) to $p_i = 3p_j$ (2B) tilts the location of the fixed points as expected (Eq. 9). Despite the change in evolution, some of the basic principles in the even-symmetry case still apply. The broken symmetry is clearly displayed in the differing evolution of each component. The component with a greater contribution to the Eq. 7 is clearly the component that races towards its fixed point more rapidly, where the component with lesser contribution takes more time to stabilize.

While the evolution is highly dependent on $\delta\omega$, ω_1 ω_r, and Δp_{ij}, a simplistic model can be presented to provide insight behind the parameter-sensitive dynamics. The evolution of the entire system can be understood by simple independent analysis of each component. The evolution of the component with larger contribution to Eq. 7 will experience a feedback field that is primarily dependent on itself. As a result, its evolution is going to be largely independent of the lesser component, which has only a minor contribution to Eq. 7. The development of a stable fixed point for a singular component in the presence of feedback field has been previously characterized [9], and so it is expected that the larger component will rapidly attempt to stabilize itself in the lowest-energy configuration.

The evolution for the component with lesser contribution to Eq. 7 will experience a different environment. Because the lesser component has only a minor contribution to the feedback fields, it will be predominantly influenced by the evolution of the larger component. Once the larger component reaches its fixed point, the feedback fields become largely static and so the lesser component evolves under a new effective field with a new effective Rabi frequency $\omega_1' = \sqrt{\omega_1^2 + (\Delta p_{ij}\omega_r)^2}$, where the diminished

strength of the feedback fields can be given by $\omega_r' = p_j\omega_r$. Since $\omega_1' \gg \omega_r'$ the imbalance in the Rabi cycle is not very significant, and so the lesser component requires a significant number of cycles in order to reach the fixed point on the opposite side of the Bloch sphere. This shift in fixed points in the transverse plane is in good agreement with the approximation set forth in Eq. 9, as shown by the solid vectors in each panel.

As was the case when $\Delta p_{ij} = 0$, the number of cycles required can be reduced by increasing ω_r, as can be seen in Fig. 2C. As expected, this comes at the expense of rotating the fixed points further away from $\omega_1 \hat{I}_x$, again in agreement with prediction. Conversely, the fixed points can be tilted back towards $\omega_1 \hat{I}_x$ by increasing ω_1 as can be seen in Fig. 2D. This increase in ω_1 further reduces the imbalance in the Rabi cycle, and consequently increases the number of required cycles before reaching the fixed points predicted in Eq. 9. While the model is crude, the evolution for each individual component can be predicted with reasonable degree of accuracy. The location of each set of fixed points can be manipulated with the competitive nature between ω_1 and ω_r, as well as the amount of time required to reach the fixed points.

The joint interaction of the CW with the feedback fields would thus be expected to generate significant contrast between two components with only a slight difference in magnetic susceptibility or resonance offset, provided the CW is placed on resonance with the average of the two components, and $\omega_1\tau_r \sim 1$. The performance of using a CW with the active feedback circuit at 300MHz with a micro-imaging probe can be seen on the imaging of a mouse with an early tumor, grown on its right leg. The appearance of the tumor in the image (Fig. 3F) shows up much clearer than it does in the other forms of conventional imaging (3A-D). The supposed susceptibility difference between the healthy

and tumor tissues would thus be expected to be visible in a susceptibility weighted image (SWI), which weighs certain parts of an image by the acquired phase during a free evolution of the magnetization prior to acquisition. From the SWI (Fig. 3E) image, it is difficult to determine the location of the tumor from simply applying the phase mask. One explanation is because there are specific limitations in producing an effective high-frequency filter in the creation of the SWI. Unless the change in resonance offset is rapid enough (constructed from high frequency components in Fourier space), any phase change in the magnetization runs the risk of being filtered out as background inhomogeneity. This can be remedied by allowing for longer evolution times to acquire more phase separation, at the expense of signal dephasing from T_2^* decay as well as phase wrapping of the magnetization, which requires additional imaging processing algorithms to handle the aliasing artifacts. While susceptibility information may be available from processing phase information, that sort of approach does not appear to be very robust as there are multiple concerns in the post-processing of the phase data.

3.4 CONCLUSION

The dynamics surrounding the evolution of a sample in the presence of feedback fields has been examined for simple two-component systems. The phase difference between both components can be encoded into the phase of the sample magnetization, and measured via standard MRI techniques. Understanding the quantum dynamics and how to manipulate them can be useful for imaging purposes where the relaxation behavior of the sample destroys the long term stability of the fixed points. Despite the destructive nature of relaxation, the system will still evolve in such a way as to minimize the total energy of the system. As a result, the dynamics en route to the fixed points can still be useful for imaging contrast as each component is seen to repel each other because of the passive/active feedback fields. The use of a CW in the presence of feedback fields can thus be used to highlight regions or tissues with only a slight difference in magnetic susceptibility or resonance offset. The amplitude of the feedback fields can be arbitrarily set to interfere with the CW in such a way as to optimize the contrast. In vivo MR images from mice cancer models suggest that this new approach successfully finds early-stage tumors more consistently than the other conventional imaging modalities, including conventional susceptibility weighted imaging.

3.5 FIGURES

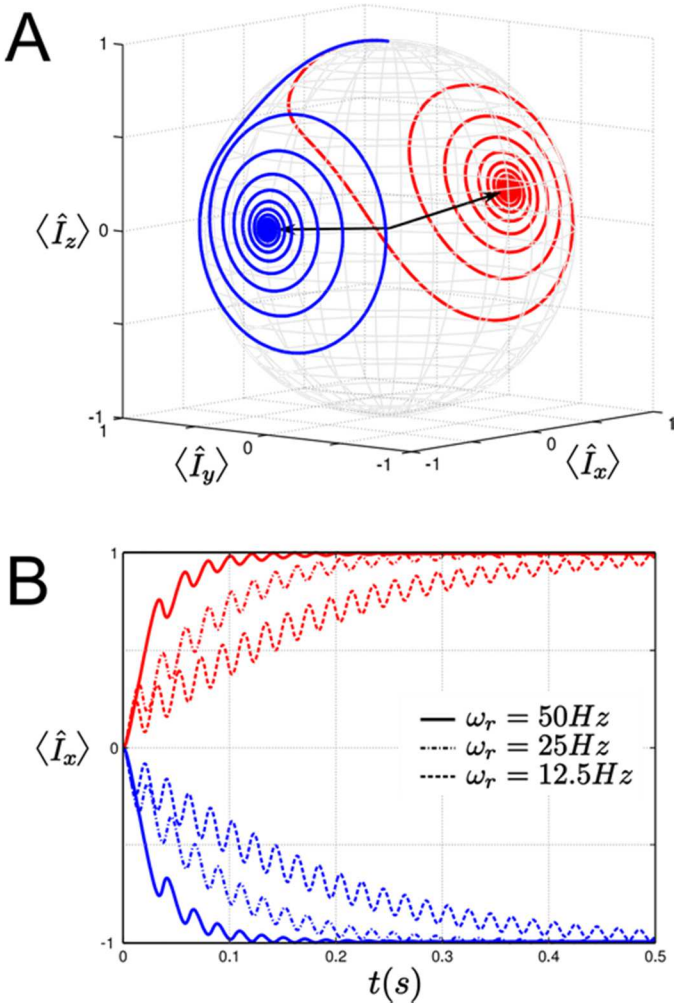

FIG. 1: Simulations showing the effect of different feedback field strengths on the development of the constants of motion. **A.)** 3D trajectory (corresponding to the 3 observables, $\langle \hat{I_x} \rangle$, $\langle \hat{I_y} \rangle$, and $\langle \hat{I_z} \rangle$), for each of the individual components of the density matrix, $\hat{\rho}(t)$ with $\omega_1 = 50$Hz, $\omega_r^{-1} = \tau_r = 20$ms, and $\delta\omega_{i/j} = \pm 5$Hz in radial frequency units. The black arrows show the orientation of the fixed points, corresponding to the $\hat{\rho}_{-+}$ state, as predicted in Eq. 6. **B.)** Evolution of $\langle \hat{I_x} \rangle$ for each component of $\hat{\rho}(t)$ with the same ω_1 and $\delta\omega_{i/j}$ as in **A**, with variable values for ω_r.

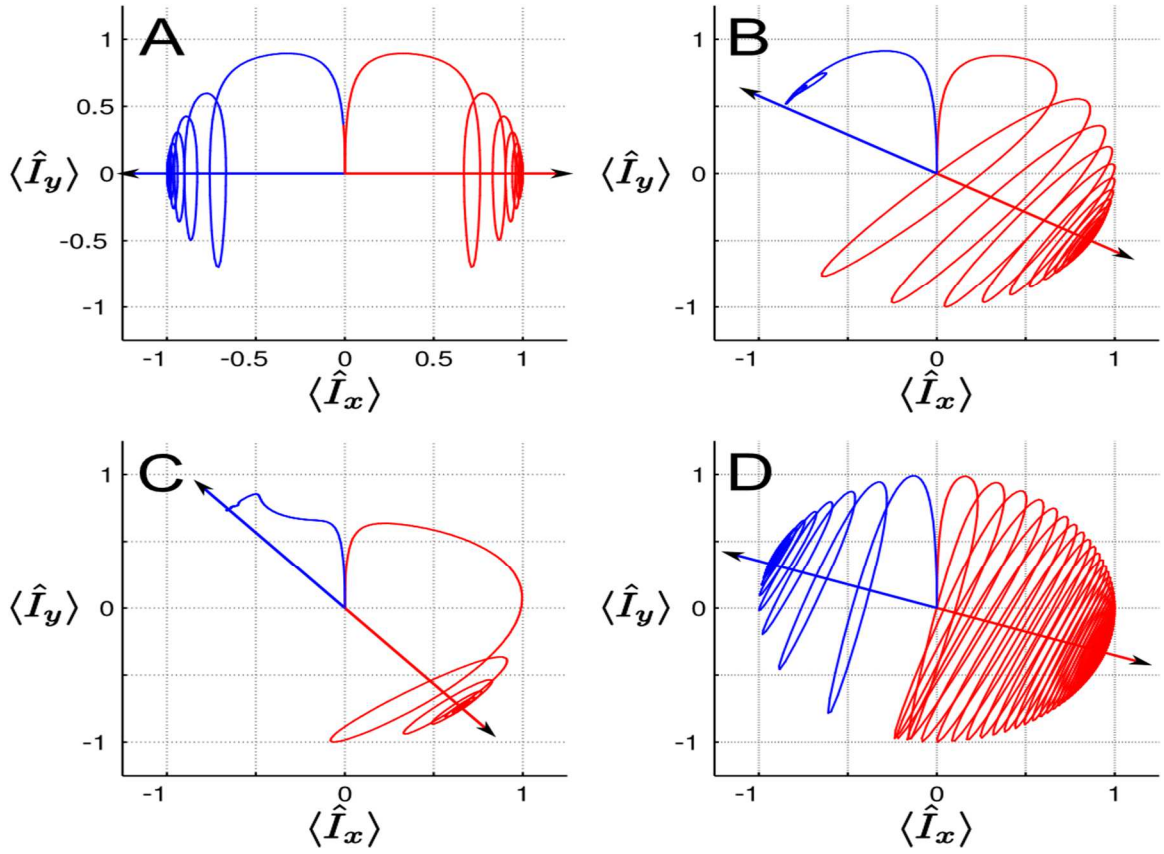

FIG. 2: 2D trajectories, showing the off-diagonal terms of $\rho\hat{}'(t)$ (corresponding to $\langle I_x^{\wedge} \rangle$ and $\langle I_y^{\wedge} \rangle$, where **A.)** ω_1 = 50Hz, ω_r = 50Hz, and $\delta\omega_{i/j}$ = 5Hz, and $p_i = p_j$, **B.)** ω_1 = 50Hz, ω_r = 50Hz, and $\delta\omega_{i/j}$ = 5Hz, and $p_i = 3p_j$, **C.)** ω_1 = 50Hz, ω_r = 75Hz, and $\delta\omega_{i/j}$ = 5Hz, and $p_i = 3p_j$, **D.)** ω_1 = 75Hz, ω_r = 50Hz, and $\delta\omega_{i/j}$ = 5Hz, and $p_i = 3p_j$, all in radial frequency units. The arrows correspond to the $\rho\hat{}'_{-+}$ state as predicted by Eq. 10.

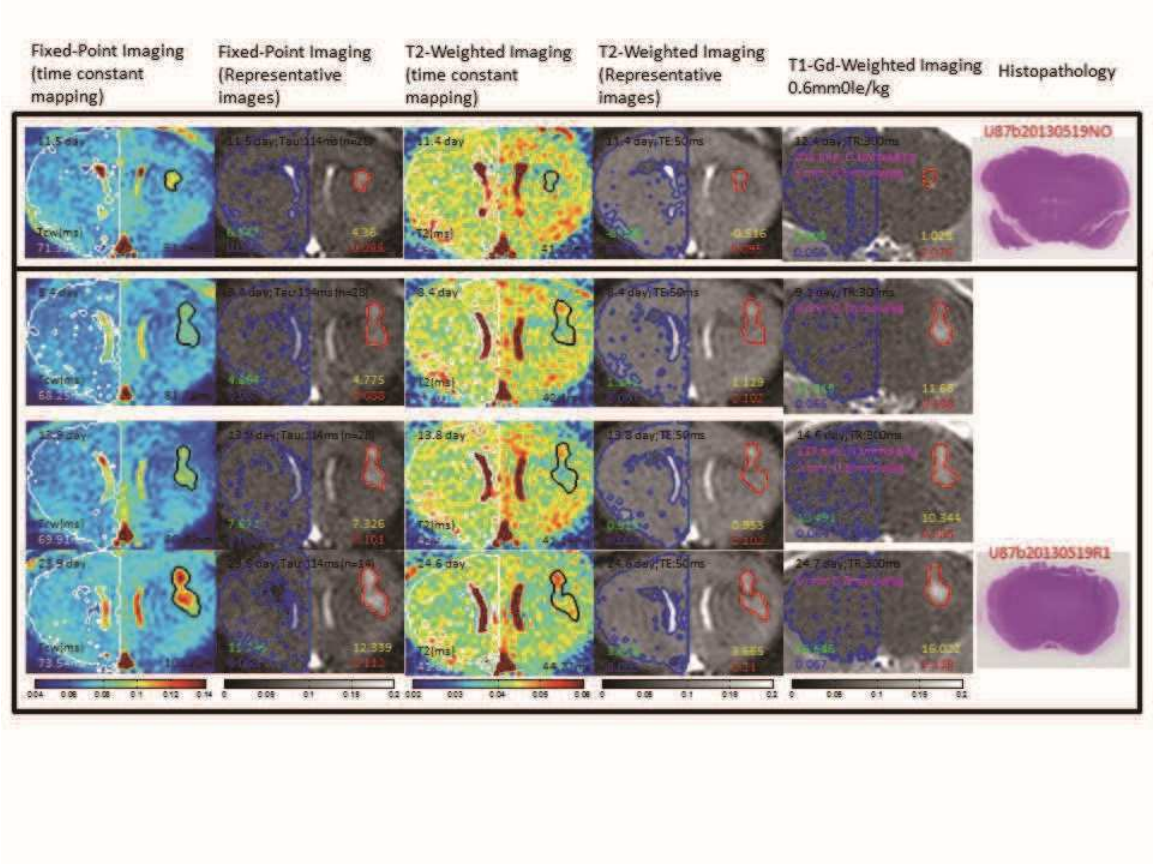

FIG. 3: Representative results from 5 mice. While T_2 parameter images (3rd column), T_2-weighted images (4th column), and T_1-Gd-weighted images (5th column) could not successfully locate the early brain tumor, the deoxyhemoglobin-based active-feedback fixed-point images (2nd column) and decay constant mapping (1st column) successfully highlight the early brain tumor with a close correlation with histopathology (6th column).

3.6 REFFERENCE

[1] E. Haacke, R. Brown, M. Thompson, R. Venkatesan, Magnetic Resonance Imaging: Physical Principles and Sequence Design (Wiley, 1999).

[2] G. Brownell, W. Sweet, Nucleonics 11, 40 (1953).

[3] W. S. Warren, et al., Science 281, 247 (1998).

[4] S. Datta, S. Y. Huang, Y.-Y. Lin, J. Phys. Chem. B. 110, 22071 (2006).

[5] S. Y. Huang, J. K. Furuyama, Y.-Y. Lin, Magn. Reson. Mater. Phy. 19, 333 (2006).

[6] S. Y. Huang, et al., Magn. Reson. Med. 56, 776 (2006).

[7] N. Bloembergen, R. V. Pound, Phys. Rev. 95, 8 (1954).

[8] S. Bloom, J. Appl. Phys. 28, 800 (1957).

[9] W. S. Warren, S. L. Hammes, J. L. Bates, J. Chem. Phys. 91, 5895 (1989).

[10] Y.-Y. Lin, N. Lisitza, S. Ahn, W. S. Warren, Science 290, 118 (2000).

[11] R. R. Ernst, W. A. Anderson, Rev. Sci. Inst. 37, 93 (1966).

[12] R. R. Ernst, G. Bodenhausen, A. Wokaun, Principles of Nuclear Magnetic Resonance in One and Two Dimensions (Oxford Science, 1987).

[13] G. P. Jones, Phys. Rev. 148, 332 (1966).

[14] I. I. Rabi, Phys. Rev. 51, 652 (1937).

[15] J. D. Walls, Y.-Y. Lin, Solid State Nuclear Magnetic Resonance 29, 22-29 (2006)

CHAPTER 4

Quantum Fixed-Point Spin Dynamics in Active-Feedback MR*

Shang-Lin Tsai, Guan Wang, Zhao Li, and Yung-Ya Lin

*This work is still in preparation to submission; further details will be included later.

Department of Chemistry and Biochemistry,

University of California, Los Angeles, CA, 90095, USA

4.1 Introduction:

In previous works [1, 2], it was successfully shown that under the weak continuous wave (CW) irradiation, an additional passive feedback field of radiation damping will act onto the sample and produce unique stable fixed points or constant of motions. The magnetization of spin ensembles will evolve to these stable fixed points as they relax through longitudinal and transverse relaxation. The study of the dynamic of fixed points can enhance the contrast of magnetic resonance imaging (MRI) in two ways. One is allowing the almost indistinguishable signal of tumor cell to evolve to different fixed points with the surrounding healthy cell and enlarge the difference between the two. The other one is that, by application of designed pulse sequence, the reactionary feedback field can be used to accelerate the magnetization back to +z position which dramatically shorten the Free Induction Decay (FID) and improve the contrast to noise ratio (CNR). In addition, it has also been shown that the contrast of MRI is improved and can be used in early detection of tumors in mice by using these fixed-points spin dynamics [3].

In this work, it is mainly focus on the study of the spin dynamics of the active feedback field in which a better way of rf pulse can be designed later and further improved the contrast of MRI. For a conventional MR machine, there are three major controllable parameters for rf pulse which includes the intensity, position, and duration of the pulse. To investigate the effect of the fixed-point spin dynamic, a homebuilt active feedback-controlled electronic device can be used to generate, amplify and shift the receiving signal further control the active feedback field. There are four chapters in this work. In the first chapter, we discuss the physical origin of the fixed-point spin dynamic and the radiation damping by controlling the intensity of rf pulse. It is critical to

understand the effect of the strength of feedback field as it is competed with the applied constant field and generated the position of the fixed points. In the second chapter, we will turn our focus on discussing the radiation damping which produced by uneven components case and multiple components case. It will be shown that instead of a single fixed point, the magnetizations for more than two spin ensembles will perform as constant in motions as they evolve in magnetic resonance. In the third chapter, it is important for us to enlarge the number of spin ensembles to meet the realistic case. From the previous brain model [4], an approximation of the dipolar field or the resonance offset from the Larmor frequency can be summarized by Gaussian distribution. Based on the distribution, hundreds of spin ensembles will be generated and evolved under the active-feedback field, and the average magnetization will be examined. In the last chapter, we will include the phase factor on the active feedback field and propose a new method to manually control the position of the fixed points. In addition to that, potential future applications by emulating the time-dependent radiation damping field will be discussed. All of the simulation results in this work are presented by numerical calculation using the MATLAB software (*The Mathworks, Natick, Massachusetts*).

Chapter 4.2

4.2.1 Theory and the Energy States

The Hamiltonian of a spin system can be given by the static and interaction Hamiltonian

$$\hat{H}_{total}(t) = \hat{H}_0 + \hat{H}_I(t) \qquad [1]$$

where the static Hamiltonian is just the Zeeman interaction, $\hat{H}_0 = \hbar\omega_0\hat{I}_z$, $\hbar$ is the Planck constant and ω_0 is the Larmor frequency. The hat symbol, ˆ, is representing the use of operator, and it will be drop for convenient. The interaction Hamiltonian, H_I, includes the perturb weak-applied radio-frequency field and the contribution from resonance offset factor, $\delta\omega$. The self-diffusion factor of the spin particle is not included in this work.

$$H_I = \hbar\omega_1(e^{-iI_z\omega_0 t}I_x e^{iI_z\omega_0 t}) + \hbar\delta\omega I_z \qquad [2]$$

Under simple unitary transformation, $U(\mathrm{t}) = e^{iI_z\omega_0 t}$, the evolution of the density operator can be transformed into Dirac picture and summarized by Liouville-von Neumann equation

$$\frac{\delta\rho^*(t)}{\delta t} = -\frac{i}{\hbar}[H_I^*,\ \rho^*(t)] \qquad [3]$$

where ρ represents the density operator under the Hamiltonian. The asterisk symbol represents the Dirac picture, and it will be dropped as rest of the discussion are within the picture.

Warren et al [5] has previous shown the unexpected dynamic of radiation damping for single spin system and the shifted fixed point under the application of CW pulse. In here, two and more spin systems will be solved simultaneously within the appropriate frame of reference.

For two spin components with the subscript of i and j, the constants of motion can be easily solved by setting Eq. 3 to zero. The relevant four constants of motion can be determined as individual Hamiltonian vectors of two spins that lies either parallel or anti-parallel to the total interaction Hamiltonian. Such ρ_{++} is the state for both components to be parallel to the effective field, and ρ_{--} is for both components to be anti-parallel to the field. Also, ρ_{+-} and ρ_{-+} states have one component aligned parallel and one component aligned anti-parallel to the field. Without any additional factor, the magnetizations of individual spin will evolve to its lowest energy state, ρ_{++}, such that the energy is given by $E_{ij} = Tr\,[\,\rho_{ij}, H_{ij}]$. Where Tr represents the Trace of the matrix.

4.2.2 Feedback Field and Radiation Damping

In the presents of the active feedback field, a semi-classical term will be added into the interaction Hamiltonian, and the trajectory of magnetization will be changed by the radiation damping.

The radiation damping and the electronic feedback magnetic field can be model as a time-dependent evolution, given by

$$H_{FF}(t) = \sum_u \hbar\omega_r(\Re\left[e^{-i\varphi}\langle iI_u^+\rangle(t)\right] I_x + \Im\left[e^{-i\varphi}\langle iI_u^+\rangle(t)\right]I_y) \qquad [4]$$

where ω_r is the strength of the passive/active feedback field, $\Re$ and $\Im$ represent the real and imaginary components of the term. φ is the tuning-dependent phase factor of the applied radiation damping, and it is assumed to be zero in this chapter. $\langle iI_u^+\rangle$ is the coupling ladder operator and is given by, $\langle iI_u^+\rangle(t) = ip_u\,Tr[I_u^+\rho_u(t)]$. where p_u is the probability of the spin component, and u is the running index of the spin components. In

the two spin component system (spin i and spin j), $p_i + p_j = 1$. Without any tuning phase, a complex rotation $\langle iI_u^+ \rangle$ is applied such the feedback field is applied 90 degree out of phase or perpendicular to the total transverse magnetization, $\langle I^+ \rangle$, which is defined as $\sum_u p_u \langle I_u^+ (t) \rangle$. Using Eq. 2 and 4, the total interaction Hamiltonian can be summarized by $H_I'(t) = H_I(t) + H_{FF}$

$$H_I'(t) = \hbar\delta\omega I_z + \hbar\omega_1 I_x + \sum_u \hbar\omega_r (\Re\left[e^{-i\varphi}\langle iI_u^+\rangle(t)\right] I_x + \Im\left[e^{-i\varphi}\langle iI_u^+\rangle(t)\right] I_y) \quad [5]$$

From Eq. 5, the effective field will be controlled by three components, ω_1, ω_r, and δ_ω. In the limit of strong radio damping, $\omega_r \sim \omega_1$, the feedback field will in direct competition with the uncoupled interaction Hamiltonian since they are applied perpendicular to each other. (shown in Eq. 4) In another word, the transverse magnetization, $\langle I^+ \rangle$, is parallel to H_I but perpendicular to H_{FF}. Energetically, the feedback Hamiltonian term in Eq. 5 will raise the total energy for both ρ_{++} and ρ_{--} states, and the fixed points will no longer holds. However, as the feedback-field term increase, the system will naturally adopt the configuration that minimize the overall transverse magnetization, $\langle I^+ \rangle$, and reduce H_{FF}. The situation is different for ρ_{+-} and ρ_{-+} states; with one spin parallel and one spin anti-parallel to each other in the transverse plane, the energy cause by feedback field or Eq. 4 will be cancel out by the two spins. Consequently, the states, ρ_{+-} and ρ_{-+}, are more favorable in thermodynamic perspective. Figure 1A shows a 3-dimensional trajectory for a two-component system with $\Delta\omega_{ij} = | \delta\omega_i - \delta\omega_j | =$ 10 Hz evolve from a static equilibrium to the fixed point. The fixed point is corresponding to the ρ_{-+} states as expected.

4.2.3 Role of Field Strength

The rate for spin systems to evolve to fixed points depend on the amount of the imbalanced of Rabi cycle. Without feedback field, the time, $\tau_1 = (2\omega_1)^{-1}$, that is required to excite the magnetization away from its initial state has the same time scale as the time, τ_2, for the magnetization to relax back. However, with the feedback field, the radiation damping destructively interferes with the CW field when being excited away from initial state, ρ_0, and constructively interferes with the CW when being returned to initial state. The imbalance Rabi cycle results in increasing the time scale of τ_1 and reducing the time scale of τ_2. In here, since both spins have a slightly resonance offset, it can be seen that the difference in τ_1 and τ_2 time scale allows a net phase accumulation after each Rabi cycle. Therefore, the magnetization of spins will naturally flow to the fixed points. As shown in Fig. 1B, increasing in ω_r with constant ω_1 rise the strength of feedback field and enlarge the imbalance of Rabi cycle. Generally, with higher ω_r, there will be a greater phase accumulation for each Rabi cycle, and the system can evolve toward the fixed point at fewer rotation. Similarly, as shown in Fig. 1C, increasing in ω_1 with constant ω_r raise the number of inversion which excites magnetization away or toward the initial condition. Consequently, it requires more cycle to reach the fixed point. In the limit that radiation damping is negligible such ω_r is approaching zero or ω_1 is approaching infinity, the feedback term in Eq. 4 and 5 will generally be vanished, and the effective field for the two components system will be reduced to Eq. 2. As shown in Fig. 1B and C, without the imbalance in Rabi cycle, the fixed-points are no longer exist and the magnetization cannot evolve towards them. Therefore, it can be seen that the condition of $\omega_r \sim \omega_1$ must be meet for the constants of motion to develop. In Fig. 1D, increasing the difference in

resonance offset allows the spins rotate faster in the transverse plane, and a greater phase can be accumulated at each cycle. As a result, the overall time scale for the system to evolve to fixed points will be shorter. However, as the increasing of resonance offset be larger than a certain limit, a direct competition between ω_1, ω_r, Δp and δ_ω will shift the location of fixed points away from the ρ_{+-} or ρ_{-+} states, and it will be discussed in the next chapter.

Chapter 4.3

4.3.1 Two Spin System with Uneven Contribution

Understanding the fixed point spin dynamics for even-component cases is useful to extend the idea to uneven-component cases or more realistic cases. With the difference in contribution between spin i and j not equal to zero ($\Delta p = |p_i - p_j| \neq 0$), the energy by feedback field in the state ρ_{+-} or ρ_{-+} will not equal to zero, and the state will no longer be the lowest energy state as Eq. 4 predicted. Thermodynamically, the system will evolve to a new fixed point with a shift of state ρ'_{+-} *or* ρ'_{-+} which depends on a direct competition between ω_1, ω_r, Δp and δ_ω. The radiation damping from Eq. 4 rotates the effective field away by a certain angle, θ_r. The degrees of rotation can then be simplified by assuming $\sqrt{\omega_1^2 + (\Delta p \omega_r)^2} \gg \delta\omega$. Despite the fact that the feedback field is perpendicular to the transverse magnetization, the total energy must be minimized when $\langle I^+ \rangle \parallel (H_I + H_{FF})$. From the geometric point of view, the rotation angle can be approximate as

$$\theta_r \cong tan^{-1}\left[\frac{\Delta p_{ij}\omega_r \cos(\theta_r)}{\omega_1 - \Delta p_{ij}\omega_r \sin(\theta_r)}\right] = sin^{-1}\left[\frac{\Delta p_{ij}\omega_r}{\omega_1}\right] \quad [6]$$

As the difference in contribution between two spins increase or the stronger the radiation damping is, the new fixed point will be tipped further away from its original fixed point. Conversely, by increasing the strength of the CW field, the tipping angle can be reduced, and the new fixed point will be closer to the original fixed point.

Fig. 2A shows the transverse projection on xy plane for a two-component system with different ratio of contribution to Eq. 4. The two spin ensembles have equal magnitude but different direction of resonance offset. i.e. $\delta\omega_i$ = 5 Hz and $\delta\omega_j$ = -5 Hz.

The probability for spin i and j are 75% and 25% respectively. The larger contribution of the i component to Eq. 4 allows the spin to evolve more likely as a single component system which has been previously described by Warren [5]. Or it can be understood as the evolution pathway of the larger contribution to the feedback field experience the field that is primarily depend on itself. As a result, the component that races towards its fixed point more rapidly. For the spin system with smaller probability to the feedback field, however, it will be a different story. The evolution of the spin system will be strongly influenced by the larger component. Since the time for the bulk component to reach its fixed point is relatively early, it is not sufficiently enough for the smaller component to reach the fixed point. Once the larger component stops evolving, the radiation damping created by it will then turn into a static vector, and the new effective field will be gradually change by the small contribution of the other spin. Consequently, as the spin system with smaller contribution experiences the new effective field, its own radiation damping will start to appears to influence its evolution path and brings the magnetization toward fixed point on the opposite of the Bloch sphere. Therefore, it will take more cycles for the spin to evolve.

4.3.2 Multi Spin Systems and CW position dependent

The dynamics of multi spin system will generally be the extension of the uneven component cases. In here, we split the minor component, spin j, in the uneven case of Fig. 2A further into two smaller components (spin j and k), and the resonance offset for the new minor components are separated by a few Hz. As shown in Fig. 2B, the evolution

path for the bulk component is almost identical to the uneven case, and the spin system has larger contribution to the feedback field and reaches to its fixed point in a faster rate. It can be seen that the two minor components will still evolve towards the opposite of Bloch sphere since each component has some contribution to the effective field. Although the coupling between two minor components evolve under strong radiation damping which contributed by bulk component is insignificant, the coupling effect can be notified after the effective field contributed by strong damping becomes constant vector. (or after the bulk component reaches the fixed point.) It can be understood easier by comparing Fig. 2B and C. Since the two minor components have different resonance offset, the amount of phase accumulate during each Rabi cycle will be different. The evolution time for each spin system to reach its fixed point will be based on a direct competition between ω_1, ω_r, Δp, δ_ω, and relative position after the strong radiation damping. By taking a closer look on spin j of Fig. 2C, it can be found that the spin will evolve to its fixed point at first; however, as the strong contribution of feedback field from bulk component become a constant vector, the new effective field which contributed by spin j and k will bring the magnetization a little bit backward to accommodate and couple with spin k. Thermodynamically, the coupling between spin j and k will prevent these spin systems to evolve to the fixed point; instead, they will perform as constants of motion.

Another interesting point from Fig. 2C is that the position of the CW field contribute to a significant role in the evolution time scale. The parameters for Fig. 2C is identical to Fig. 2B with only a 3 Hz shift of the position of CW field to the right. As shown in both Fig. 2C and D, the shift of CW field will effect similarly as decreasing the

resonance offset of the bulk component and increasing in the minor components. As shown previously, the decrease in resonance offset reduce the amount of phase to accumulate at each Rabi cycle. Therefore, the bulk component will need more time to reach to its fixed point. However, for the minor components, the larger resonance offset allows them to evolve to their fixed points or constants of motion at faster rate. The overall evolution times for all three spin systems can be reduced by a shift of CW field as shown in Fig. 2D. Conversely, by controlling the position of CW field, it is possible to increase the evolution time of one spin system and decrease the other kinds of spin systems, and it is possible to enlarge the contrast between the two.

Chapter 4.4

4.4.1 Multi Spin Systems and Spin Distribution

Multi spin systems will be considered as a more practical way to realistic situation, and the average spin dynamics will be recognized as a representation of all. From previous study [6], it was found that the tumor tissue will have a slightly different micro condition than the surrounding healthy cells. In particular, as brain cancer, multi form of glioblastoma, grow, the surrounding blood vessel density will drop, and the size of blood vessel will increase. One of the well-known functional MRI method, Blood Oxygenation Level Dependent (BOLD), uses the relative distance between hydrogen particle and blood vessel to determine the relative resonance offset of the particle. Since the deoxyhemoglobin inside the blood vessel is paramagnetic and able to generate a local field to the surrounding particles, the induced local field will act constructively or destructively to these hydrogen particles and differentiate their resonance offset. By simulating thousands of particles, the distribution of the resonance offset can be approximated by a Gaussian distribution.

In here, 201 spin ensembles are simulated with the resonance offset from -100 to 100 Hz, and the spin dynamic of the multi spin system is summarized by averaging each spin components with the corresponding weighting factor from the Gaussian distribution. As shown in Fig. 3A, the fact of having both positive and negative resonance offset spin components balance out the magnetization in x-direction since each spin component will flow to either side of Bloch sphere. However, it can be easily seen that the average spin system reaches a constant of motion after evolving through a certain numbers of cycles.

From the BOLD model, it is known that the resonance offset distribution for tumor cell is different than the healthy one. Here, we propose four different kinds of distributions of the dipolar field and study the effect of changing the position of CW field as shown in Fig. 3B. The results are presented in Fig. 3C and D. The constant of motion is defined as the degree of fluctuation in all directions of the magnetizations stop changing in magnitude. As predict in section 4.2.3, the spin system with broader resonance offset distribution (i.e. larger standard deviation (SD)) has a greater phase accumulation during each Rabi cycle, and it is able to evolve to the constant of motion at shorter time. Conversely, the spin system with narrower resonance offset distribution generally need to rotate more cycle before reaching to its constant of motion since the amount of phase accumulate in 1 cycle is small. For example, the spin system with the distribution, SD = 50 Hz, can reach to its constant of motion at about 0.2 second, but the one with SD = 2 Hz will need over 0.5 second.

Similar to section 4.3.2, the position of the CW field is also considered with the case of multiple spin systems. In Fig. 3D, the CW field for a spin system with normal distribution (SD = 18 Hz) will be placed in center (blue), 10 Hz to the left (orange), and 30 Hz to the left (green) respectively. As the CW field move away from the center, the dipolar field for each spin component increase; thus, the evolution time to the constant of motion will be shorter. The presence of the imbalance field distribution also rotates the location of the constants of motion away in an angle which is described by Eq. 6. In the strong resonance offset case, the tipping angle cannot described by the equation since the original assumption, $\sqrt{\omega_1^2 + (\Delta p \omega_r)^2} \gg \delta\omega$, breaks. The new tipping angle will be based on the direct competition between ω_1, ω_r, Δp and δ_ω.

Chapter 4.5

4.5.1 Time Dependent Fixed Points

Previously, the phase, φ, of the active feedback source was set to 0 for the purpose to understand the spin dynamic; in here, the controllable phase factor will open a new page for the ability to dynamically control the location of the fixed point in real time. Similar to the discussion in section 4.3.1, the imbalance contribution of two spin systems increases the energy of the ρ_{+-} or ρ_{-+} states, and the system will adopt to a new state to reduce the overall energy which depends on ω_1, ω_r, Δp, δ_ω. With the additional phase factor, from Eq. 4, the phase joins the competition to reduce overall energy. The rotation angle which tips the fixed point away will no longer be Eq. 6 and will be given by a geometric approach

$$\theta_r = cos^{-1}\left[\frac{\sqrt{\omega_1^2-(\Delta p_{ij}\omega_r\cos(\varphi))^2}}{\omega_1}\right] \quad [7]$$

In general, as the phase approach to zero, it can be seen that Eq. 7 will converge to Eq. 6. Also, by setting $\varphi = \pi/2$, Eq. 7 will lead to a zero-degree rotation of the tipping angle, $\theta_r = 0$, and the system will be assumed to evolve to the fixed point identical to the one without spin contribution difference (fixed points in Fig. 1A). However, as discussed in section 4.2.3, the radiation damping is controlled by ω_1, ω_r, Δp, δ_ω. with additional phase factor. Trivially, allowing ω_1 to approach to infinity or ω_r to approach to zero will destroy the radiation damping and leads to no fixed point as can be seen in Eq. 4. Similarly, setting $\varphi = \pi/2$, the feedback field will be parallel to the transverse

magnetization, and it cannot produce an imbalanced Rabi cycle, which is needed to reach the fixed points.

The story of the above approach tells that the system cannot reach to a certain fixed points because the factor of ω_1, ω_r or φ all have the effect of minimizing the imbalanced Rabi cycle. However, our team proposed a two-step time-dependent fixed-point scheme which has the ability to move the fixed points to any desire location after the initial fixed point has been reached. As shown in Fig. 4A, step 1 occurs when the spin system evolves to its fixed points with no phase factor. Once the system has reached to the fixed points, a gradual perturbation of the values of ω_1, ω_r or φ can be made. Since the perturbation is infinitesimally small, the system can reach to a new fixed points gradually without the needed of strong imbalanced Rabi cycle. In our case (step 2), immediately after the system reach to its fixed points, φ is gradually increased to $\varphi = \pi/2$ together with gradually increasing ω_1. From Eq. 7, it can be seen that the rotation angle, θ_r, of the new fixed-points is slowly decrease to zero, and eventually, the system will rotate to the state which is similar to the one without contribution difference. As a result, the study of fixed points dynamics allows the system to evolve and follow in a specific trajectory to any desire positions in Bloch sphere.

4.5.2 Self Nutation

Self nutation refers as the case that the system can be designed to evolve towards fixed points along the ± z axes by controlling the active feedback source. Despite the fact that the natural radiation damping will be active whenever Eq. 4 is not equal to zero, the

active feedback device has the advantage to control on and off of the feedback field and ability to control the phase to rotate to the magnetization in any desired direction.

In here, a two-step time-dependent fixed-point scheme is performed as shown in Fig. 4C. For a two spin system with opposite sign of resonance offset and different contribution, a preparatory 90° pulse brings both magnetizations to the +x direction. Without any feedback field, spins are allowed to freely evolve on transverse plane for a certain time period, τ_1. Then, the feedback field is applied onto the system by activating the feedback device. With the controlled phase (here φ = 100), the feedback signal is applied directly between both components, and the spins are deviated from the transverse plane and evolved in the opposite directions along the z-axis. It can be seen that the trajectories depend heavily on both τ_1 and φ. Also, the evolution time to reach the fixed points is sensitive to the specific phase angle of the applied feedback signal, as shown in Fig. 4D.

4.6 Conclusion

In this work, we first introduce the dynamics of magnetization evolutions for two-spin systems under the presence of the feedback field, and we gradually include the contribution factor and talk about the continuous multi-spins systems. Despite the nature of relaxation, the contribution of feedback field will change the total energy for every states, and the spins will eventually evolve to a new fixed points to minimize energy, Eq.4. As a result, even for a very small difference in resonance offset can allow the system to flow to the opposite sides of the Bloch Sphere and create a sufficient contrast for imaging. Furthermore, we have shown that by using our new proposed two-step time-dependent fixed-point scheme, the location of fixed points can be governed in a way to maximize the contrast of MRI. In particular, the controllable phase factor by our active feedback device allows the magnetizations flow toward ±z direction. Therefore, the dynamics *en route*, which is controlled by ω_1, ω_r and φ, to the fixed points, thus become an important task for the future pulse sequence design. As our goal in this paper is to summarize those factors, we can show the development of stable fixed points can open a new page in future MRI technique.

4.7 Figures

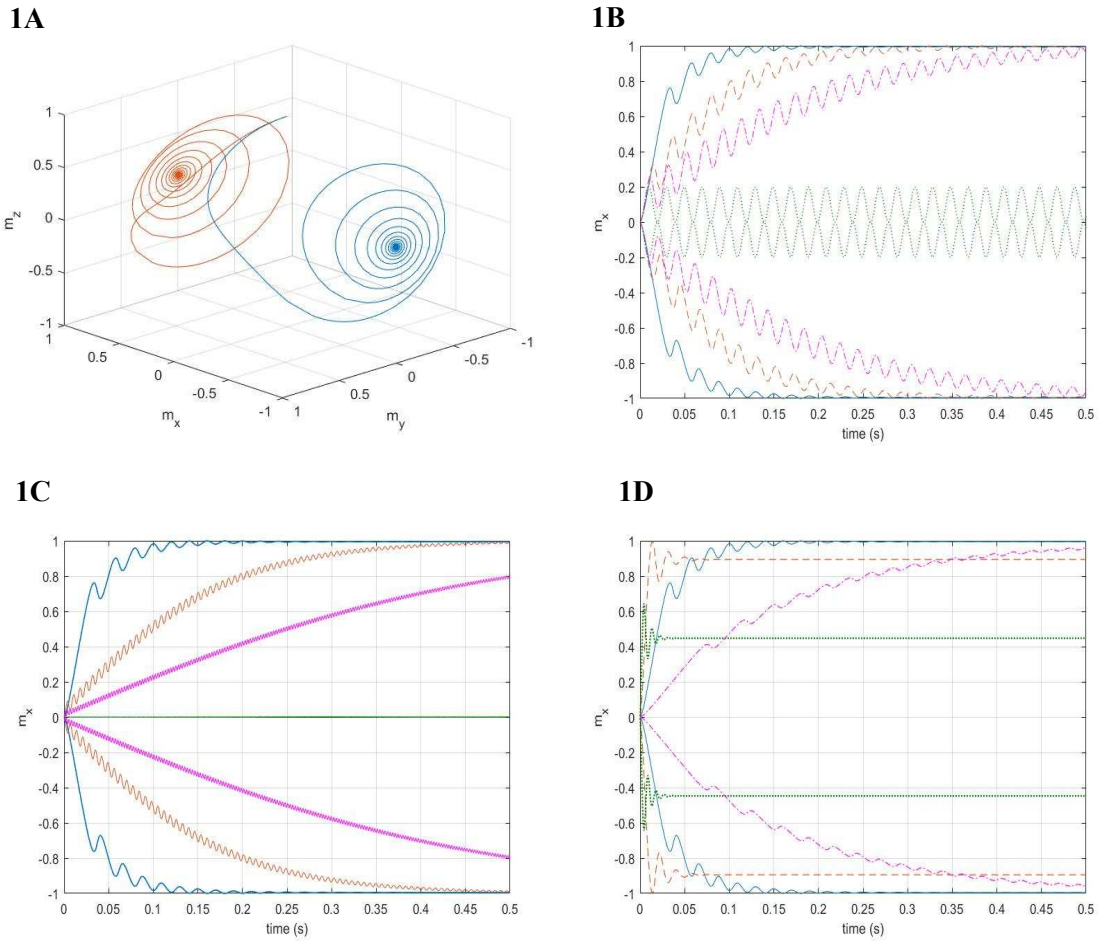

FIG. 1. **A.)** 3-dimensional trajectory for a two-component system, where the resonance offset $\Delta\omega_{ij}$ = 10 Hz. The position of continuous wave is set to be at the center where $\delta\omega_i$ = - $\delta\omega_j$ = 5 Hz. The strength of CW and feedback field are set to be $\omega_1 = \omega_r$ = -50 Hz. All input variables are needed to convert into angular frequency for accuracy. **B.)** Feedback field dependent with adjustable ω_r = -50 (blue), -25 (orange), -12.5 (magenta), and approximate to 0 (green) Hz. **C.)** Continuous wave field (CW) dependent with ω_1 = -50 (blue), -150 (orange), -350 (magenta), and approaching infinity (green) Hz. **D.)** Difference in resonance offset dependent with $\Delta\omega$ = 2 (magenta), 10 (blue), 50 (orange), and 200 (green) Hz.

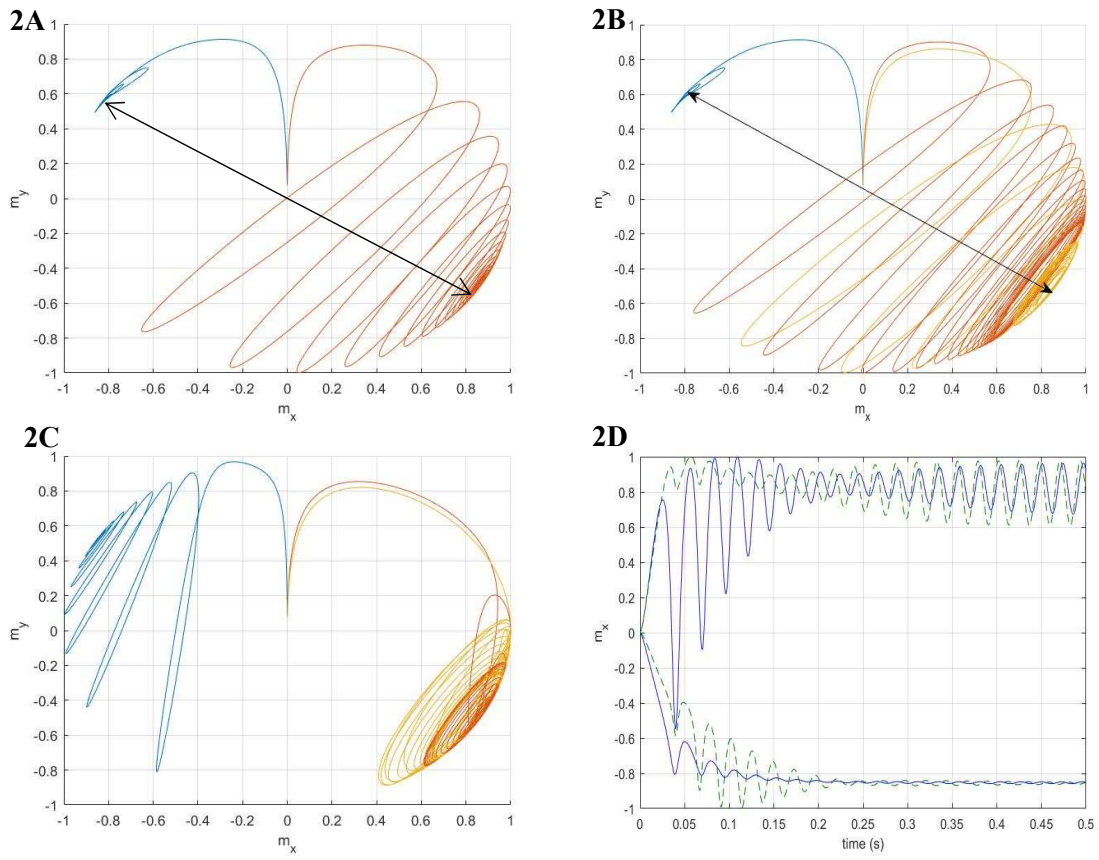

FIG. 2. **A.)** Transverse projection on xy plane for a two-component system with different ratio of contribution to Eq. 4. $\Delta\omega_{ij}$ = 10 Hz, $\omega_1 = \omega_r$ = -50 Hz. The CW field is placed on the center with $\delta\omega_i$ = - $\delta\omega_j$ = 5 Hz, and the ratio of contribution between i, j spins are 3:1 respectively. **B.)** Transverse projection on xy plane for a three-component. $\omega_1 = \omega_r$ = -50 Hz. The CW field is placed on the center with $\delta\omega_i$ = 5 Hz, $\delta\omega_j$ = -4 Hz, and $\delta\omega_k$ = -6 Hz and the ratio of contribution are 6:1:1 respectively. The difference between the bulk component and the average of the two minor components is 10 Hz apart as 2A. **C.)** A similar setup as part B with 3Hz shift of position of CW field to the right. The new resonance offset is thus $\delta\omega_i$ = 2 Hz, $\delta\omega_j$ = -7 Hz, and $\delta\omega_k$ = -9 Hz. **D.)** A comparison of x component magnetizations on i and j spin between part B (solid blue) and C (dash green).

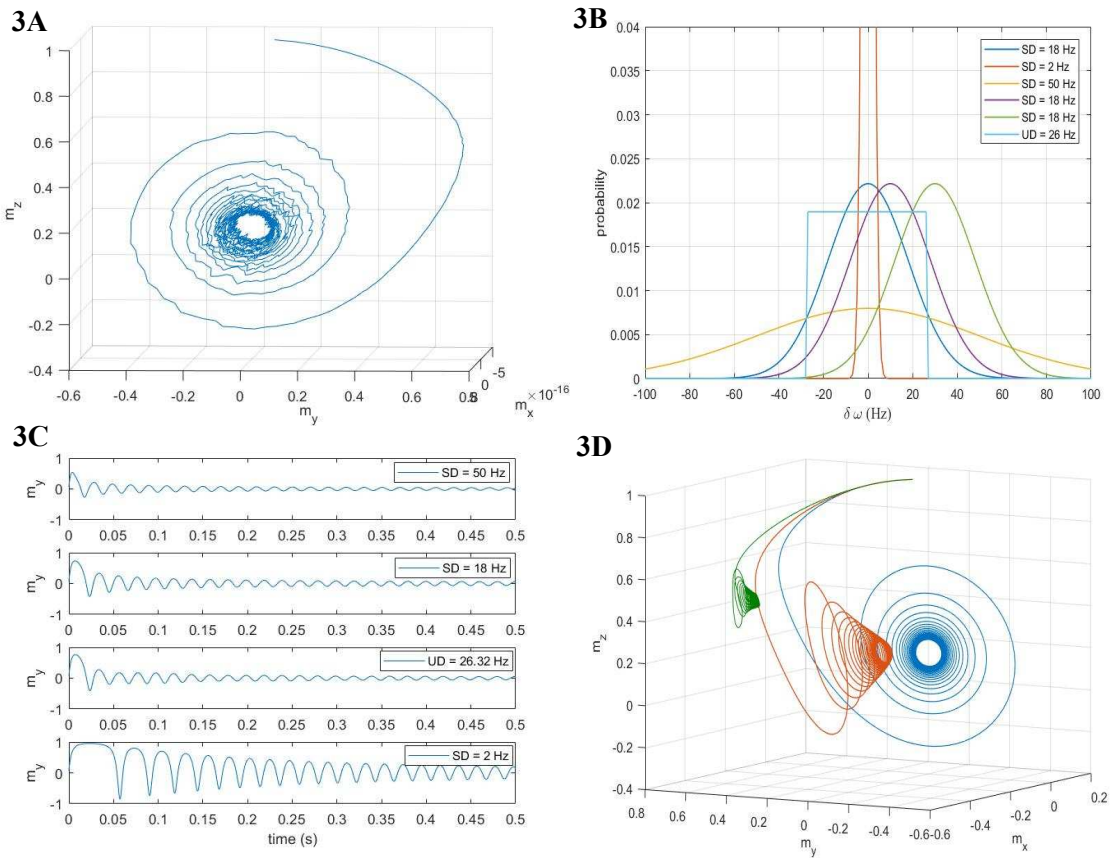

FIG. 3. **A.)** 3-dimensional trajectory for an average of 201 spin ensembles from $\delta\omega$ = -100 to 100 Hz with probability equal to Gaussian distribution with standard deviation (SD) equal to 18 Hz. **B.)** A summary of the probability distribution chart. Three Gaussian distributions with standard deviation (SD) equal to 18 Hz (blue), 2 Hz (orange), and 50 Hz (yellow). 10 Hz shift of CW field to the left (purple), 30 Hz shift to the left (green) of Gaussian distribution with SD = 18 Hz. Also, a uniform distribution equals 1.896% between ± 26.32 Hz is shown as (cyan) **C.)** A time evolution of y component of magnetization with different kinds of distribution. **D.)** 3-dimensional trajectory from average of 201 spin ensembles with different positions of CW field. SD = 18 Hz (CW position at center for blue, -10 Hz for orange, and -30 for green.)

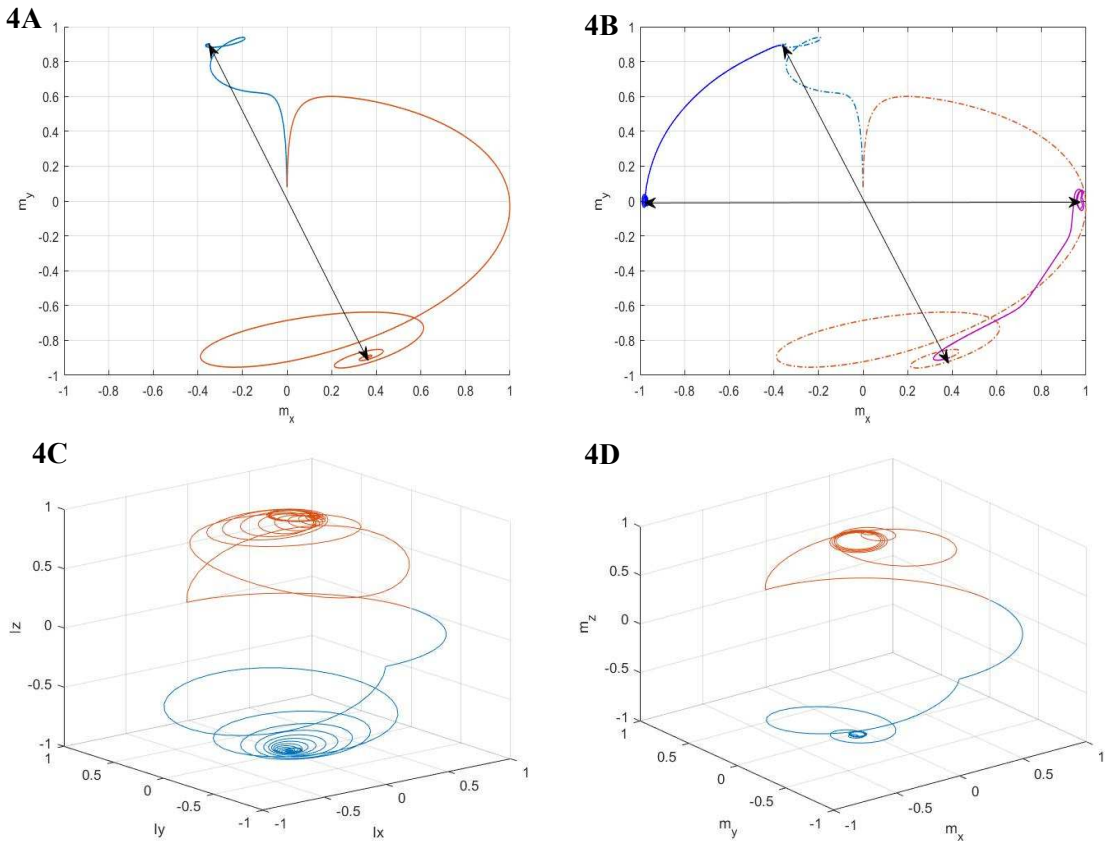

FIG. 4. Transverse projection of the two-step evolution for the system $\delta\omega_i$ = - $\delta\omega_j$ = 5 Hz with the ratio of contribution of 4:1. ω_1 = -50 Hz and ω_r = -80 Hz. **A.)** step 1 is a simple application for a system in the presence of radiation damping to evolve to the fixed-points. **B.)** The second step involves the slowly increment of active feedback phase φ, from 0 to $\pi/2$, and gradual increase of the strength of CW to -200 Hz. This figure demonstrates the theoretical ability to control the location of the fixed points in real time. **C.)** A self-nutation experiment starts from a 90° pulse followed by a free evolution time, τ_1. As the two spins have different resonance offset, the magnetization of individual spin will precess away from each other. The Feedback signal is then turned on with a specific phase, φ, such that the feedback field is applied between both components. These two spins will evolve in opposite directions towards ± z directions. The parameters are set as

$\delta\omega_i$ = - $\delta\omega_j$ = -5 Hz with the ratio of contribution of 3:1. ω_1 = -20 Hz. The phase of active feedback source will be turned on after τ_1 = 50ms, and φ is chosen to be 100°. **D.)** 110°. The self-nutation experiment shows the capability for controlling the evolution of spin dynamic under active feedback source, and the dramatic reduction of relaxation time to ± z directions.

4.8 Reference

[1] Abergel D. Chaotic solutions of the feedback driven Bloch equations. Phys. Lett. A. 2002; 302(1): 17-22.

[2] Vlassenbroek A, Jeener J, and Broekaert P. Radiation Damping in High Resolution Liquid NMR: A simulation study. J. Chem. Phys. 1995; 103: 5886.

[3] Furuyama JK, Hwang DW, Huang SY, Walls JD, Chang HW, Hwang LP, Lin YY. Dynamic Fixed-Point Generation Using Non-Linear Feedback Fields – with Applications in MR Contrast Enhancement. MRM. 2009; 65-78.

[4] Wang G, Tsai SL, Li Z, Hsu CH, Lin YY. Detection of Early Glioblastoma Multiform in Orthotopic Xenograft Mouse Models: Numerical Simulations and *In Vivo* Experiments. (In preparation of publication)

[5] Warren WS, Hammes SL, Bates JL. Dynamics of Radiation Damping in Nuclear Magnetic Resonance. J. Chem. Phys. 1989; 91: 5895.

[6] Valable S, Lemasson B, Farion R, Beaumont M, Segebarth C, Remy C, Barbier EL.

Assessment of Blood Volume, Vessel Size, and the Expression of Angiogenic Factors in two Rat Glioma Models: a longitudinal in vivo and ex vivo study. NMR Biomed 2008; 21: 1043-1056.

CHAPTER 5

Conclusion and Future Outlook

During my two years Master Degree study in Department of Scholar Program in Chemistry, I set my goal to advance the understanding of tumor detection on its early stage. With the help from my mentor, professor Yung-Ya Lin, and others, I chose my path to specialize in biophysical chemistry to extend my knowledge on identifying diseases, especially by using Magnetic Resonance Imaging (MRI). In particular, based on the commonly used fMRI method (blood oxygenation level dependent), we (my group member and I) defined the model of one of the most dangerous brain tumor, Glioblastoma Multiform, by its aggregation effect during the early stage. Via Monte Carlo simulations from three different kinds of pulse sequences, the resulting relaxation constants of our tumor model showed good agreement with the *in vivo* experimental results. We concluded the difference in relaxation time constants between the tumor cell and its surrounding is partially reasoned as a competition between two diffusing regimes: Static Dephasing Regime (SDR) and the Motional Averaging Regime (MAR). Secondly, we proposed an enhancement method of MRI signal by introducing the use of the active feedback field. With the homebuilt electronic device to retransmit the phase factor back to the system based on the receiving signal, the feedback field will increase the energy of its original state, and the system will naturally evolve into a new state or fixed points, thermodynamically. Therefore, by using the CW field, the regions with a slight difference

in magnetic susceptibility can be highlighted in MRI. Lastly, we proposed a detail spin dynamics of the active feedback field. The evolutions of multi spin-system and unbalance spin-system can be further understand as more realistic cases. Furthermore, we presented the possibility of using two-step time dependent active feedback field to control the locations of fixed points and enhance the MRI signals.

With the strong foundation of the spin dynamics under active feedback field, I feel more confident on my goal which is the enhancement of tumor detection. Thus, for my short term research direction, I will incorporate the model of early brain tumor cell and the evolution under active feedback field to simulate a more realistic spin system and to develop a better pulse sequence for tumor detection. As for my long term goal, I will extend the use of the spin dynamics to different kinds of tumors other than glioblastoma multiform to target the existence and locations of the lesions. Finally, with the well-define tumor-detection method, I believed varied MR Nano medicines can be developed and helped millions of people.